Photoelectron spectromicroscopy and spectronanoscopy at synchrotrons: Growing impact on life sciences and materials science

G. Margaritondo

Ecole Polytechnique Fédérale de Lausanne (EPFL), CH-1015 Lausanne, Switzerland

ARTICLE INFO

ABSTRACT

We review the historical and recent development of experimental techniques that are based on the combination of photoemission spectroscopy and high lateral resolution. The discussion specifically deals with the essential features of the two main classes of approaches in this domain—scanning spectromicroscopy and the techniques based on electron optics. Selected examples are presented to illustrate the exceptional capabilities made possible by the technological advances of recent years. The article is concluded by a short discussion of the foreseeable future of this fast-developing field.

© 2009 Elsevier B.V. All rights reserved.

1. Historical background

The keyword in the title of this review, "spectromicroscopy", is self-explanatory: it refers to a broad class of experimental techniques that combine the analytical power of spectroscopy with high spatial resolution. The advantages over mere spectroscopy are evident: in many cases, the important properties probed by spectroscopy change from place to place—and key phenomena can be confined to small areas. Therefore, spectroscopy probing wide regions often misses crucial elements and can even be misleading.

For many types of spectroscopy, high spatial resolution could not be achieved until quite recently. This was specifically true for spectroscopy techniques based on synchrotron and free electron laser sources of photons [1,2]—such as photoemission or X-ray absorption. One or two decades ago, such sources were already much better than their classical counterparts but not good enough to combine spectroscopy with high lateral resolution.

In the mid-1980s, a new technical evolution initiated and rapidly led to new levels of performance for both synchrotron sources and infrared free electron lasers [1,2]. Spectromicroscopy – and later spectronanoscopy – was one of the most important historical consequences of this progress.

The progress was quantitatively measured [1] in terms of the parameter *B* called brilliance or brightness. Roughly speaking [1,3], this parameter is proportional to the flux *F* emitted by the source and inversely proportional to both of its transverse emittances ε_x and ε_y. In turn, ε_x is proportional to the source size σ_x and angular

spread θ_x in the *x*-direction—and ε_y is likewise proportional to $\sigma_y\theta_y$. Therefore:

$$B \propto F(\sigma_x\theta_x\sigma_y\theta_y)^{-1}. \tag{1}$$

For decades, the progress in the synchrotron brightness was primarily due to the steady decrease in the geometric parameters, σ_x, θ_x, σ_y, θ_y, obtained by improving the electron beam control. The Liouville theorem requires the quantity $(\sigma_x\theta_x\sigma_y\theta_y)$ – which is proportional to the transverse phase space volume – to be constant. Therefore, strong focusing to decrease $\sigma_x\sigma_y$ implies an increase in angular divergence. The practical consequence is that high spatial resolution is easier if $(\sigma_x\theta_x\sigma_y\theta_y)$ is small. That is why high brightness obtained by decreasing $(\sigma_x\theta_x\sigma_y\theta_y)$ facilitated the transition from spectroscopy to spectromicroscopy.

A low emittance, however, is not sufficient for spectromicroscopy without a sufficiently high photon flux. Indeed, the transition from spectroscopy to spectromicroscopy became feasible in the second half of the 1980s thanks to the advent of undulator sources [1,2] with high flux and brightness. Until then, most synchrotron beamlines received photons from the bending magnets that keep the electrons in a closed trajectory within a storage ring.

The synchrotron emission is strongly confined by relativistic effects [1–3] to the forward direction of the electron motion in the ring. Therefore, at each passage in a bending magnet an electron "illuminates" the beamline only for a short period of time. This short duration corresponds to a large bandwidth of frequencies (or wavelengths). During monochromatization as required for specific applications, most of the flux is filtered out and the actually used flux and brightness are rather limited.

In an undulator, a rather long periodic array of magnets forces [1–2] the electron to gently oscillate in a transverse direction. The

---

E-mail address: giorgio.margaritondo@epfl.ch.

emission of photons takes place during the entire passage of the electrons along the magnet array. The illumination of the beamline occurs for a longer period of time than on the case of bending magnets—and the frequency (or wavelength) bandwidth is much narrower. Even after monochromatization, the flux is large and the brightness very high. This makes it feasible to perform spectroscopy with high spatial resolution.

Photoemission is a very good example of the evolution [4] from spectroscopy to spectromicroscopy. Only more than five decades after Einstein developed its conceptual background [1], did the photoelectric effect start to be actually used for physical and chemical analysis. The reason for this long delay was primarily the short elastic mean-free-path of excited electrons in solids—that confines to the near-surface region the emission of photoelectrons. To avoid artifacts due to contamination, the analyzed surface must be ultraclean and kept under ultrahigh vacuum. Photoemission spectroscopy became really feasible only with the advent of ultrahigh vacuum technology.

The analytical capabilities of photoemission spectroscopy were remarkable but the lack of lateral resolution was a severe handicap. The limited brightness of conventional photon sources and of the early synchrotron sources did not allow analyzing surfaces smaller than several square millimeter. The studies were therefore blind to all the important properties and features occurring on a smaller scale. For example, it was virtually useless for biological systems whose benchmark for lateral resolution is the size of cells.

Three more decades were needed to overcome this severe obstacle. Although important precursor work took place in the 1970s and early 1980s (see, for example, the excellent review of Turner et al. [5]), only in the mid- and late 1980s did the notion of photoemission with high lateral resolution truly evolved from dream to reality [4]. The early steps took place in different institutions, including the Wisconsin Synchrotron Radiation Center (SRC) [6,7], HASYLAB in Hamburg [8], NSLS in Brookhaven [9], SSRL in Stanford [10], ALS in Berkeley [11] and MAXLAB in Lund [12].

High lateral resolution was achieved with either one of the two complementary approaches [4]—see Fig. 1. In the first case, the photoelectron–exciting photon beam was focused into a small lateral area so that photoelectron emission was confined to it. This
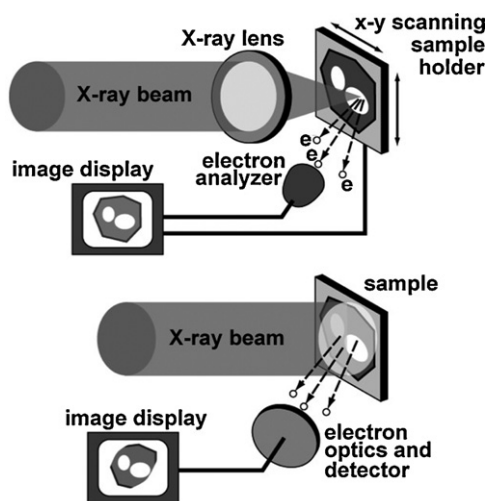
made it possible to take photoemission spectra for small regions. The most direct application was to analyze the core-level peaks and derive local chemical properties like the presence of the elements corresponding to the detected core levels or, with a more refined analysis, their chemical bonding status.

It was also possible to obtain chemical "maps" by detecting the intensity of a given core-level peak while scanning the focused photon beam over the sample surface (or, more practically, the sample with respect to the beam). One could thus see the distribution of elements and of their chemical status. Likewise, by detecting valence spectral features from small areas or by monitoring their intensity while scanning the focused beam over the surface one could analyze fine chemical and physical properties over a local scale and the corresponding two-dimensional maps.

The second approach of Fig. 1 does not strictly require focusing and can be implemented even if the X-ray beam floods a relatively large area of the sample. The photoelectrons emitted from this area are processed by an electron optical system. This makes it possible to obtain images by converting the electrons into photons with a suitable two-dimensional device.

The earliest version of this approach based on synchrotron radiation was developed, notably by Tonner and Harp [6], under the name of "PEEM" (photoelectron emission microscopy). The photoelectrons in those early steps were not energy-filtered and therefore the signal was dominated by "secondary" photoelectrons. These are low-energy electrons produced by inelastic scattering events in the material after the initial electron excitation by absorption of a photon [1].

The secondary photoelectron yield was demonstrated by Gudat and Kunz [13] to be proportional to the photon absorption. Therefore, by scanning the photon energy across a core-level threshold of a given element, one could identify in PEEM images the components related to the same element. This performance is widely exploited for detailed chemical analysis of the surface region. The PEEM added [6] to this popular spectroscopic approach the lateral resolution required for a spectromicroscopy.

1.1. Acronyms and techniques

One of the main problems encountered by outsiders when they try to penetrate for the first time the world of photoemission spectromicroscopy is the rather liberal use of acronyms. We would like to facilitate the task by summarizing here the most widely used among them [14].

We already introduced "PEEM". When using photons in the X-ray region, the PEEM is often called X-ray PEEM or "XPEEM". The counterpart of PEEM – the class of techniques illustrated by the top portion of Fig. 1 – is often called "SPEM" or scanning photoemission microscopy.

The spectroscopic aspect of PEEM or XPEEM spectromicroscopy can be implemented with a variety of approaches. We already mentioned the X-ray absorption spectroscopy ("XAS") based on the Gudat–Kunz mechanism [13]. Depending on the specific photon energy region, the XAS structure can be called [1,2] "EXAFS" (extended X-ray absorption fine structure), referring to the regular oscillations well above an X-ray core-level absorption threshold. When close to the threshold, the structure is called "XANES" (X-ray absorption near-edge structure) or "NEXAFS" (near-edge X-ray absorption fine structure) [1,2]. In combination with magnetic linear dichroism (MLD) or magnetic circular dichroism (MCD), PEEM or XPEEM are excellent techniques for the study of surface magnetism [14].

Instead of scanning the photon energy, the spectroscopic aspect of PEEM or XPEEM can also be implemented by filtering the photoelectron energy rather than accepting the full photoelectron yield. An important class of instruments in this regard is the combination

Fig. 1. The two classes of photoelectron spectroscopy techniques [4]. (Top) In the "scanning" class, the primary photon beam is focused into a small sample area. Thus, photoemission spectra can be obtained with an electron analyzer for that area. By monitoring the intensity of specific spectral features while scanning the sample with respect to the focused beam in a two-dimensional fashion, one can also obtain chemical maps. (Bottom) The "electron microscopy approach": the lateral resolution is obtained by processing the emitted photoelectrons with an electron optical system.

of XPEEM and Ernst Bauer's "LEEM" (low-energy electron microscopy) [14]—called "SPELEEM" (spectroscopic photoemission low-energy electron microscope). Unfortunately, this acronym is quite similar [14] to that of the LEEM instrument that uses a spin-polarized primary electron beam, called "SPLEEM" or spin-polarized LEEM: some level of confusion for the outsiders is quite understandable.

To complete the acronym and techniques review, we would like to mention that photoemission spectromicroscopy derives from standard photoemission spectroscopy without high lateral resolution [1,2]. The different varieties of photoemission are historically known as "ESCA" (electron spectroscopy for chemical analysis), "XPS" (X-ray photoemission spectroscopy), "UPS" (ultraviolet photoemission spectroscopy), "ARUPS" (angle-resolved UPS) and others.

1.2. Early examples

A complete review of the initial results by different authors is beyond the scope of the present article that is mostly focused on recent events. We will thus limit our discussion to a few examples from our own contributions: the objective is to give a flavor of those early steps.

One of the first focusing–scanning spectromicroscope was the MAXIMUM (multiple application X-ray imaging undulator microscope) system [7,15,16]. Fig. 2(top) shows an original scheme of this system. The X-ray source was a 60-pole undulator originally developed by the Stanford Synchrotron Radiation Laboratory (SSRL) and then loaned by H. Winick to the Wisconsin Synchrotron Radiation Center (SRC), operating there on the Aladdin storage ring. The emitted photon energy ranged from 37 to 400 eV. After monochromatization, the photon beam was focused by a Schwarzschild objective, the combination of two concave and convex reflecting lens. The sample was mounted on a scanning stage that could produce images and the electrons were collected, energy-filtered and detected by a cylindrical-mirror energy analyzer.

One of the major difficulties in developing the MAXIMUM system was obtaining sufficient X-ray reflection for the two lens surfaces (the reflectivity of soft-X-rays is very low). The solution was provided by multilayer Mo/Si coating (88.7 Å periodicity) of the curved surfaces, yielding a total reflection efficiency of 25% for entire objective at a photon energy of 76–77 eV.

The middle and bottom parts of Fig. 2 show some of the early results of the MAXIMUM system [7,15]. The middle-left image was taken on a Ni grid with 25 μm periodicity by collecting electrons of all energy without filtering them (total yield mode). This image was geometrically corrected and compensated for the decay of the emitted X-ray beam intensity. The middle-right image shows a 500 Å thick Al coating of a GaAs(1 1 0) substrate; a 25 μm period mesh was put on the substrate during the overlayer evaporation. The image was again taken in the total yield mode and shows, besides the overlayer, some cleavage steps of the substrate.

The bottom part of Fig. 2 shows a test demonstrating [7] that by 1993 MAXIMUM had surpassed the 1 μm lateral resolution level. The image of a Fresnel zone plate (FZP) includes indeed 900 Å wide zones that are clearly visible. The 1 μm resolution level was corroborated by more stringent tests and demonstrated that the instrument could, for example, be useful in the study of biological systems at the cell level [7].

Fig. 3 shows results demonstrating [16] that MAXIMUM could indeed operate in the spectroscopic mode, i.e., by filtering the energy of the collected photoelectrons. The specific experiment concerned a rectangular-patterned overlayer of $In_{0.3}Ga_{0.7}As$ deposited on a GaAs(1 1 0) substrate. The top part of the figure shows photoemission spectra for the $In_{0.3}Ga_{0.7}As$ rectangles and for the visible GaAs surface between them. The As3d core-level peak is
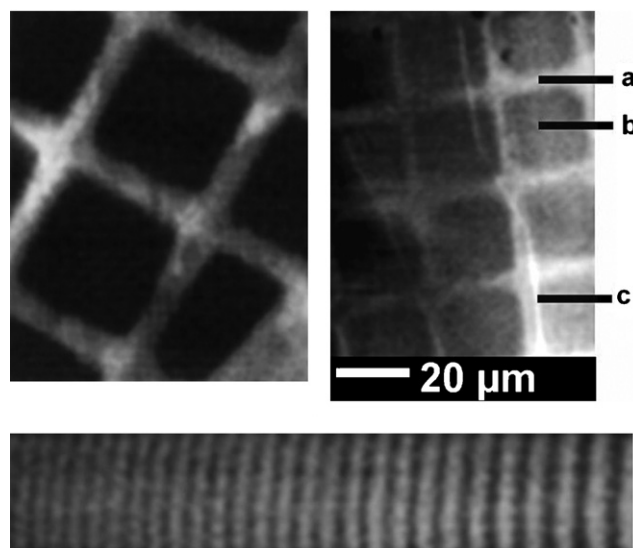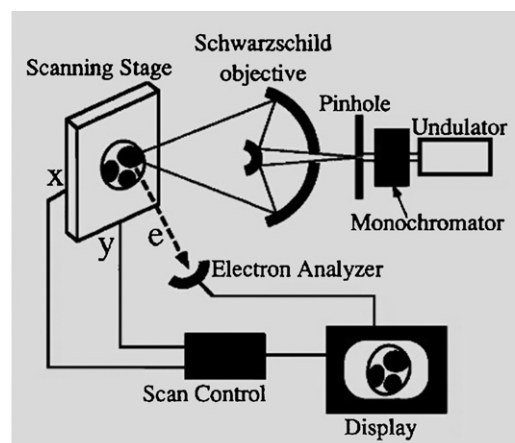

Fig. 2. (Top) scheme of the MAXIMUM system [7]. (Middle-left) MAXIMUM image of a Ni grid with 25 μm periodicity obtained by collecting the unfiltered photoelectron yield. This image was geometrically corrected and compensated for the decay of the emitted X-ray beam intensity. (Middle-right) Similar image of a patterned 500 Å thick Al coating on a GaAs(1 1 0) substrate, showing uncoated (a) GaAs, (b) Al squares and (c) some cleavage steps. (Bottom) Image of a Fresnel zone plate used as a resolution test pattern. Data extracted from Refs. [7,15].

clearly visible in both cases but the overlayer also exhibits a second peak due to oxide formation.

The bottom part of the figure shows three images taken with photoelectrons of selected energies corresponding to the As3d, Ga3d and In4d core-level peaks. The In4d image reveals the overlayer alone whereas the other two show both the overlayer and the substrate. This is a nice illustration of the capability of photoelectron spectromicroscopy, even at its early historical stage, to produce chemical maps revealing the composition and chemical binding status of the system under investigation.

We can now turn our attention to the second type of photoelectron spectromicroscopy technique illustrated by Figs. 1 and 4 shows schemes of the original PEEM described by Tonner and Hart in Ref. [6]. On the top, the general layout: photoelectrons leaving the sample are processed by a lens objective with a single electrostatic cathode. The lens includes two elements: an anode at ground and a control electrode (or Wehnelt) for focusing. The sample is kept at high negative potential (down to −10 keV) and the focusing on the image plan is obtained by tuning the potential of the control electrode.

The image is obtained at the phosphor screen by converting electrons into photons. Before reaching the phosphor screen, the
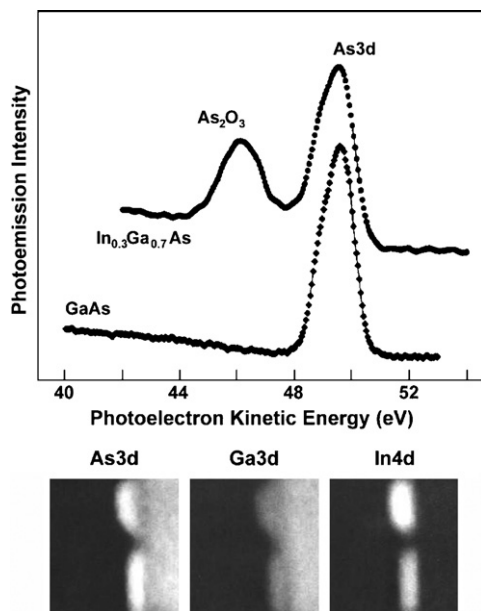
Fig. 3. Early MAXIMUM results obtained in the spectroscopic mode on a rectangular-patterned overlayer of $In_{0.3}Ga_{0.7}As$ deposited on a GaAs(1 1 0) substrate. (Top) Photoemission spectra for the $In_{0.3}Ga_{0.7}As$ rectangles and for the visible GaAs surface between them. (Bottom) Images taken with photoelectrons of selected energies corresponding to the As3d, Ga3d and In4d core-level peaks. Data derived from Ref. [16].

electron flux in each direction can be intensified by a microchannel plate (the two-dimensional version of a channel multiplier). The bottom part of Fig. 4 shows a detailed scheme of the lens itself. The construction is quite simple and includes isolating spacers and a stainless-steel cylindrical aperture holder.

Even the very first tests of the PEEM instruments demonstrated very interesting performances. The spectroscopic capabilities were linked, as already mentioned, to the tuning of the photon energy. Using this approach Tonner and Hart [6] were able, for example, to
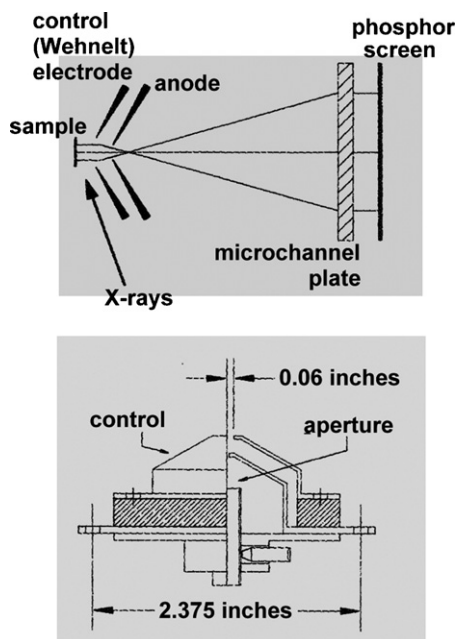

Fig. 4. Schemes of the original PEEM described by Tonner and Hart in Ref. [6]. (Top) Overall instrument layout; (bottom) details of the lens system. Figures derived from Ref. [6].

reverse the intensity pattern of the images of a partially gold-coated silicon wafer. At a photon energy of 45 eV, below the threshold for excitation and emission of Au4f electrons, the uncovered silicon parts were brighter than the Au-covered regions—whereas the situation was inverted for a photon energy of 108 eV.

Both MAXIMUM and the PEEM provided even in their initial development stages lateral resolutions interesting for biological specimens. Tests with cell specimens initiated quite early and Fig. 5 shows one interesting example obtained by G. De Stasio (now P.U.P.A. Gilbert) et al. [17].

On the top-left, the figure shows a PEEM image taken at a photon energy of 65 eV of a rat neuron culture grown for 8 days on a gold substrate. The actual objective of the experiment was not to image the neuron structure itself but to analyze the uptake of metals. After culturing, the cell specimen was washed and exposed to a metal halide—AlF_3 in the case of Fig. 5. The residual metal not uptaken by cells was eliminated, then the specimen was analyzed by PEEM to detect the spatial distribution of the metal.

The bottom-left image of Fig. 5 shows the result for aluminum and was obtained in the following way. First, two equivalent images were taken at photon energies, 74 and 78 eV, right below and above the Al2p X-ray absorption threshold. Then the two images were digitally subtracted pixel-by-pixel, thus emphasizing the regions of strong Al-related emission. These are the black portions of the bottom-left image of Fig. 5.

The result is quite striking: the uptaken aluminum is strongly concentrated in a specific portion of the culture. To emphasize this point, the Al distribution map image (Fig. 5(bottom-left)) was actually superimposed to an attenuated, edge-enhanced version of the top-left image of Fig. 5.

The link between Al and the dark parts of the distribution map image were confirmed by the spectroscopic results shown in the right part of Fig. 5. These are local X-ray absorption spectra as a function of the photon energy. Such spectra were obtained by measuring the intensity of a given part of the image while scanning the photon energy. The two curves of Fig. 5 correspond to the two points "a" and "b" of the top-left image. In the b-curve, the Al2p threshold is clearly visible, confirming the presence of this element. By contrast, the b-curve reveals no Al at all.

This result was not just a feasibility test but also an interesting finding from a biochemical point of view. The digital subtraction technique made it possible to quickly examine a large number of cells for the presence of Al. Some 10^5 cells were analyzed in such a way: only three of them revealed Al uptake. A morphological analysis indicated that all three were large-size glial cells (Purkinje neurons), quite different from the granule cells prevailing in the culture.

In general, the first tests of the mid-1990s demonstrated that photoemission had definitely overcome the special resolution limitations that prevented it from being useful in biomedical research. This conclusion was repeatedly corroborated in the subsequent years.

2. A clear case: semiconductor interface inhomogeneities

Many problems in physics, chemistry, materials science and biomedical research can take advantage of high lateral resolution in photoemission experiments. To illustrate this point, we would like to discuss here a classical issue: the lateral inhomogeneities of semiconductor interfaces [18–21].

The importance of such interfaces needs not to be emphasized: they are the backbone of the devices that constitute the foundations of microelectronics and computer hardware. These fields actually initiated their fantastic growth with the early understanding of the interface properties in devices like FETs. An even better understand-
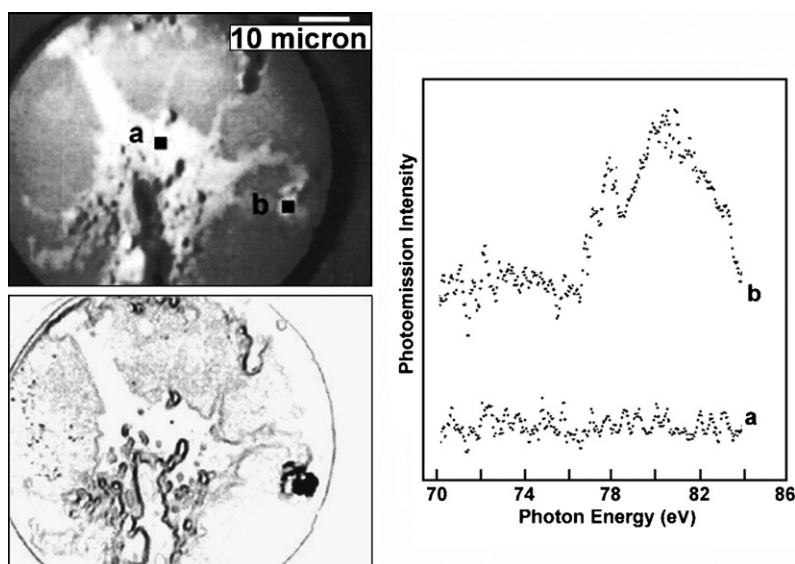
Fig. 5. (Left, top) PEEM image of a rat neuron culture over Au taken at a photon energy of 65 eV. (Left, bottom) Element map showing the distribution of Al after exposure of the culture to AlF$_3$ (the image processing procedure is described in the text). (Right) PEEM absorption spectra taken at points a and b: only for point b the Al2p threshold is present. Data derived from Ref. [17].

ing and the microscopic control of interfaces is the key for new, more performing and potentially revolutionary devices [22].

Paradoxically, the complex physics and chemistry of semiconductor interfaces did not yet fully penetrate the real world of device technology. Oversimplified ideas are still present—often giving the illusion of understanding the device behavior but really only marginally dealing with the issues. Let us, therefore, begin our discussion from some of such oversimplified textbook notions.

Fig. 6 shows elementary energy schemes of the three main classes of semiconductor interfaces: semiconductor–vacuum, metal–semiconductor and semiconductor–semiconductor (heterojunction) systems. In the top panel, the band structure of a semiconductor (with the valence band, the conduction band and the forbidden gap) is electrostatically "bent" near the interface between the semiconductor and vacuum. The reason is that the electronic structure of the semiconductor surface is not equivalent to that of the bulk and there are "surface states" that modify the local distance between the Fermi level and the band edges. Thus, there is an electron energy barrier between the Fermi level and the bottom of the conduction band at the surface. The scheme is shown for an n-type semiconductor but the case of a p-type material would be similar except for the direction of the band bending.

The middle panel of Fig. 6 shows the case of a semiconductor–metal interface, to some extent similar to the previous one. However, in the metal electrons occupy the states all the way up to the Fermi level (at absolute zero temperature). The energy barrier in this case is the "Schottky barrier" that determines the rectification properties of semiconductor–metal diodes.

The bottom panel shows the interface between two different semiconductors, A and B. There is a new element besides band bending on both sides: the difference between the two forbidden gaps must be accommodated by valence and conduction band discontinuities. Such discontinuities play a major role in the physics of heterojunction devices [22].

Conventional photoemission was used for years to analyze clean surfaces, Schottky barriers and heterojunctions [22]. The reason is the surface sensitivity of the photoelectron probe: the elastic mean-free-path of excited electrons in a solid is equivalent to a few atomic planes. Thus, photoemission spectra primarily reflect the surface electronic structure. For example, referring to the top part of Fig. 6, the edge of a valence photoemission spectrum would not reflect the bulk position of the valence band edge but that of the surface, shifted by the band bending.

Schottky barriers and heterojunctions can be studied by depositing thin films of metals or semiconductors on semiconductors
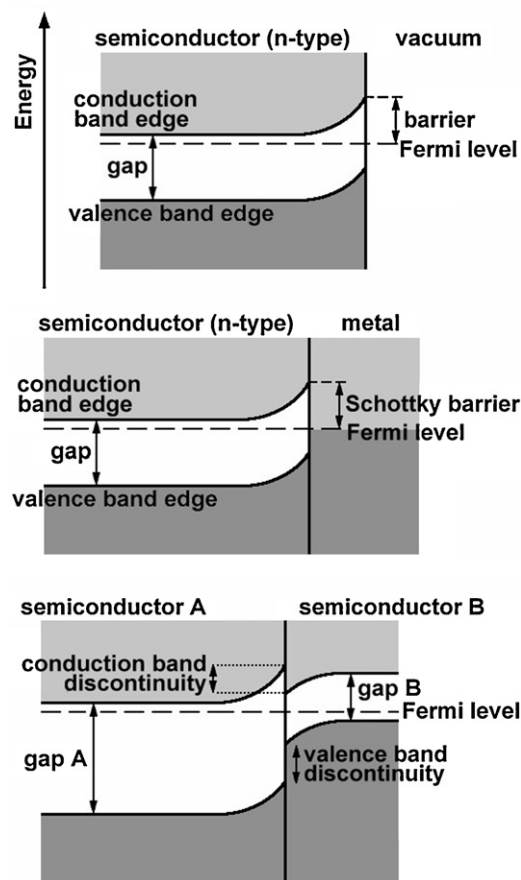

Fig. 6. Schemes of the three main classes of semiconductor interfaces. (Top) Semiconductor–vacuum interface; (middle) semiconductor–metal interface; (bottom) semiconductor–semiconductor (heterojunction) interface.
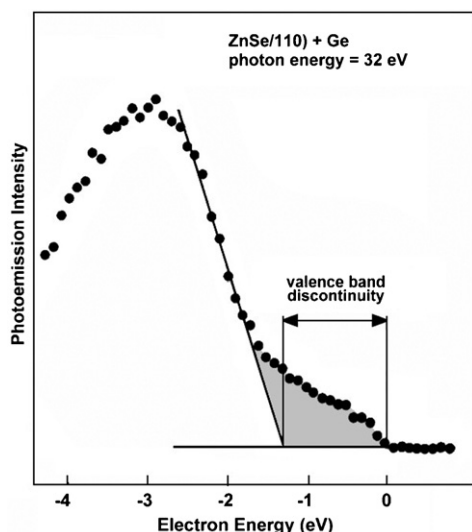
Fig. 7. Example of photoemission study of semiconductor interfaces. The valence-band photoemission spectrum of a ZnSe(1 1 0) substrate with a 5 Å thick Ge overlayer, annealed for 5 min at 280 °C, clearly show a double edge reflecting the presence of the valence band discontinuity. Data derived from Ref. [23].

substrates. By progressively increasing the overlayer thickness and taking photoemission spectra at each step, it is possible to follow the establishment of the band bending and of the other interface features.

Fig. 7 shows a classic example of this broadly used approach [23]. The photoemission spectrum refers to the energy region near the top of the valence band of a system consisting of a ZnSe(110) substrate with a 5 Å thick Ge overlayer, after annealing for 5 min at 280 °C. The spectrum clearly shows a double edge reflecting the presence of the valence band discontinuity. As schematically shown, from such a result a quantitative estimate of the valence band discontinuity can be extracted—obtaining in this case 1.35 ± 0.1 eV. The conduction band discontinuity can then be evaluated since the sum of the magnitudes of the two discontinuities (Fig. 6, bottom) equals the magnitude of the difference between the two gaps.

In other cases, the valence band discontinuity is too small to produce a double spectral edge. However, from the analysis of valence and core photoelectron spectra the discontinuities can still be derived [22]. Similarly, photoelectron spectra can yield estimates of the Schottky barrier for semiconductor–metal interfaces [24].

This brings us to the key question leading to the need for spectromicroscopy. Are interface parameters like the Schottky barriers or the band discontinuities a property of the entire interface? Are they, in other words, constant for the entire interface or can they vary from point to point?

This is a very important but largely ignored question for microelectronics. Consider, for example, a Schottky barrier: in the normal description of a semiconductor–metal rectifying diode, it is assumed that the same barrier exists for the entire interface. Conduction measurements and photoemission tests without high lateral resolution would in that case yield reliable barrier values.

Suppose, however, that the barrier is not the same for the entire interface, but, for example, smaller in 10% of it than for the rest. In the laterally averaging measurements of standard photoemission this component would be impossible to detect within the experimental uncertainty. On the other hand, conduction tests and the operation of the diode are not averaging operations: the weakest barrier would dominate. Any theory based on the assumption of a single barrier for the entire interface would thus fail to produce a realistic picture.

The aforementioned question is therefore a key one. To tackle it, standard photoemission is not sufficient and the lateral resolution of spectromicroscopy is required. How much lateral resolution? The benchmark [1,22] can be provided by the Debye length: over much smaller distances, the barrier fluctuations are smoothed out. The band bending occurs over a distance determined by this length. Thus, the lateral resolution must surpass the Debye length [22]: depending on doping, this typically ranges from tenths of microns to microns. Modern photoemission spectromicroscopy is thus adequate to attack this problem.

Spectromicroscopy tests [18–21] did answer the question: do lateral fluctuations of the semiconductor interface parameters occur? The first evidence was obtained for semiconductor–vacuum interfaces and it was positive. Consider the results of Fig. 8, obtained for a cleaved GaAs(1 1 0) surface [18]. The right-hand side shows images obtained with the MAXIMUM spectromicroscope at the same photon energy (95 eV) and at two different photoelectron kinetic energies, 70.3 and 71.3. Such energies are both close to the Ga3d core-level peak position. If the band bending was homogeneous for the entire surface, then the energy position of the peak would be the same everywhere and at each kinetic energy the image would be structureless. On the contrary, the images exhibit clear structures revealing changes from place to place of the peak position and of the band bending.
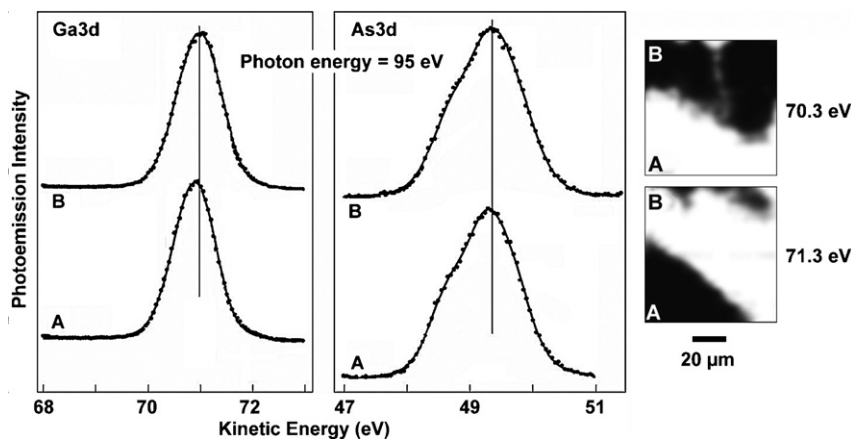

Fig. 8. Photoemission spectromicroscopy reveals the fluctuations in the band bending at a GaAs(1 1 0)–vacuum interface. (Right) images taken at two different photoelectron energies in the spectral region of the Ga3d peak. The images clearly show inhomogeneities corresponding to band bending fluctuations from point to point that change the peak position. (Left and middle) Ga3d and As3d peaks for points A and B in the right-hand images. Data derived from Ref. [18].
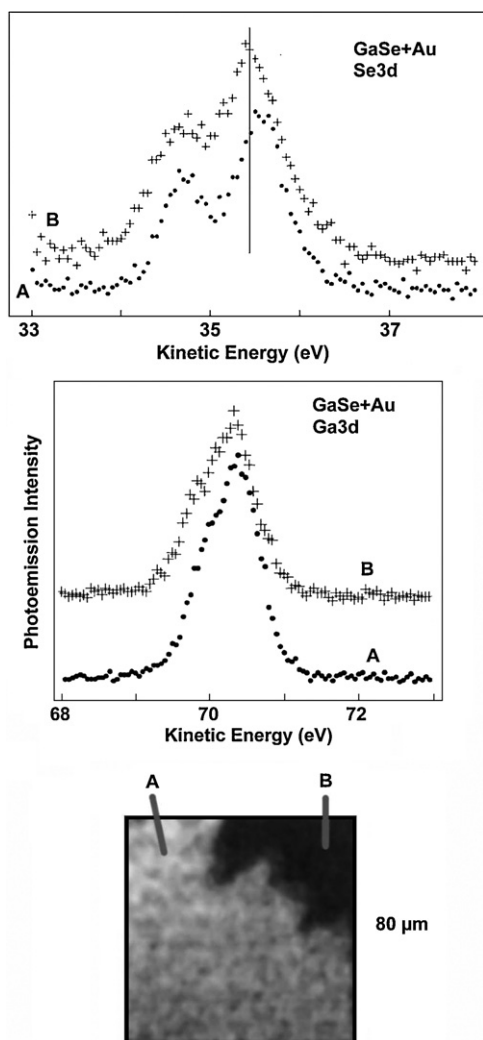
Fig. 9. Photoemission spectromicroscopy detects the lateral fluctuations of the Schottky barrier for a 2 Å thick Au overlayer on GaSe [19]. (Bottom) Image obtained with the MAXIMUM spectromicroscope at a photon energy of 95 eV and at a kinetic energy corresponding to Au5d photoelectrons. (Top and middle) Se3d and Ga3d photoemission peaks for points A and B in the images. Results extracted from Ref. [19].

The left and center sides of Fig. 8 show Ga3d and As3d core-level photoemission peaks for the points A and B in the images of the right-hand side. We see indeed that the peak positions are shifted in energy between two points by approximately the same amount for the two core levels. This corroborates the conclusion that the band bending changes from place to place.

Such results imposed a conceptual revision of the ideas about band bending and electronic structure for semiconductor surfaces. Virtually all theoretical models [22] predicted homogeneous band bending due to the pinning of the Fermi level in a given energy position inside the forbidden gap. There was significant dissent among theorists about the causes of the Fermi level pinning, but no controversy about the fact that the pinning was the same from point to point. Results like those of Fig. 8 put a question mark on the very foundations of semiconductor interface physics.

Subsequent studies revealed inhomogeneities for other classes of semiconductor interfaces, demonstrating that the case of Fig. 8 is not unique. Fig. 9 shows, for example [19], results on a semiconductor–metal interface: a 2 Å thick Au overlayer on the surface of the layered semiconductor GaSe. The bottom part is an

image obtained with the MAXIMUM spectromicroscope at a photon energy of 95 eV and at a kinetic energy corresponding to Au5d photoelectrons.

Here again the image is not structureless and reveals inhomogeneities. Core-level photoemission spectra (middle and upper parts of Fig. 9) indicate that such features are related to differences in the band bending. This is supported by the parallel shift in energy of the Ga3d and Se3d peaks taken at points A and B of the image.

As it can be realized from Fig. 6(middle), such a shift corresponds to different values of the Schottky barrier. Thus, this important parameter is not constant for the entire semiconductor–metal interface as commonly assumed in device modeling.

A similar conclusion can be reached from the results of Fig. 10 in the case of heterojunctions [20]. The system explored here is a GaSe substrate covered by one-half mononolayer of Ge. The top-left part is a photoemission spectromicroscopy picture taken again with the MAXIMUM system, by detecting photoelectrons excited by 95 eV photons at a kinetic energy of 61.2 eV—corresponding to the Ge3d core-level peak. In this case too image inhomogeneities are evident.

The right-hand curves correspond to spectra in the Ga3d, Se3d and Ge3d peak regions, taken with the same photon energy and at points A and B of the image. The substrate core-level peaks shift by the same amount on going from points A to B whereas the overlayer peak position remains unchanged.

The left-bottom part of Fig. 10 explains this result in terms of heterojunction band structure schemes similar to that of Fig. 6. Basically, the band bending on the substrate side changes between points A and B—and so does the interface position of the Ga3d core level (as that of the Se3d level, not shown). The interface position of the overlayer Ge3d level does not change. The three spectra thus demonstrate that the valence band discontinuity changes between points A and B and it is not a constant for the entire interface.

The above results raise many questions about the quality of theoretical model of microelectronic devices—as well as about the causes of the inhomogeneities. The latter issue was the subject of intense studies and the results of Fig. 11 provide a hint [21].

The spectra taken with a scanning photoemission spectromicroscope show the Si2p core-level peak for a heterojunction consisting of a GaSe substrate with a 3-monolayer coverage by Si. The spectra were taken at two different points and reveal substantial changes in the Si2p peak lineshape. Previously, the GaSe substrate was considered as chemically unreactive, with the coverage implying no chemical interactions and no chemical shifts [1] in energy of the core level. On the contrary, the lineshapes of Fig. 11 indicate reveal spectral components corresponding to different interface reacted species. And the lineshape changes from point to point reveal changes in this microchemical composition.

This result suggests that microchemistry is a factor in the fluctuation of the interface parameters. This hypothesis was corroborated by several studies but a complete understanding of the interface properties changes is still elusive. The experimental background to solve this issue strictly requires high lateral resolution in the photoemission experiments—and it constitutes an excellent case for spectromicroscopy.

3. Examples of recent progress

The best way to illustrate the spreading impact of spectromicroscopy in recent years is by practical examples. We thus discuss some interesting recent cases, without however presenting an exhaustive review. The examples provide a good idea of how powerful, sophisticated has become this class of techniques—and therefore potentially helpful for a variety of domains.
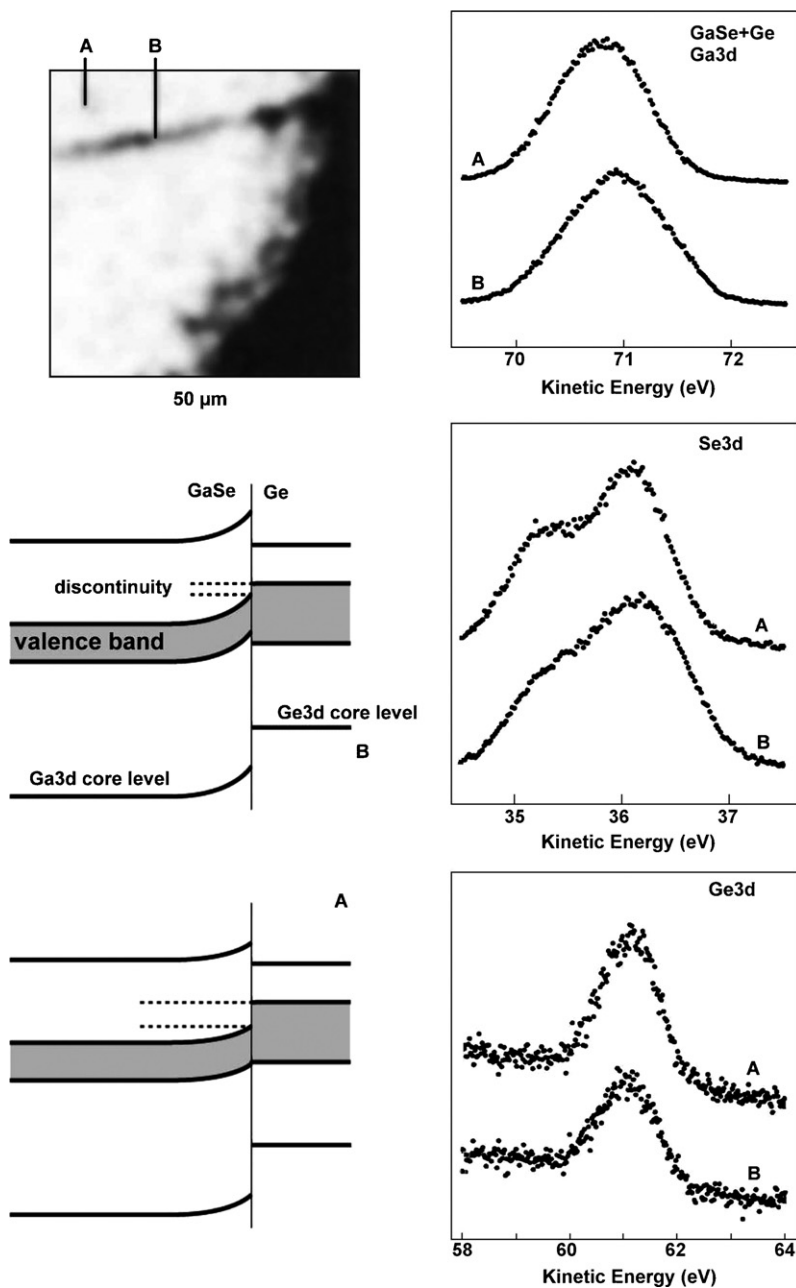
Fig. 10. Lateral fluctuations of the band discontinuities at the heterojunction interface between a GaSe substrate and one-half monolayer of Ge [20]. (Top-left) photoemission spectromicroscopy picture taken with the MAXIMUM system by detecting Ge3d photoelectrons. (Right) Ga3d, Se3d and Ge3d photoemission peaks taken at 95 eV photon energy for points A and B in the image. (Bottom left) Schematic explanation of the results in terms of changes of the valence band discontinuity. Experimental data derived from Ref. [20].

3.1. Regular patterns formed by phase separation of adsorbates

In this interesting phenomenon, different phases of an adsorbate system can spontaneously separate forming regular patterns. Fig. 12 shows a nice example by Locatelli and Kiskinova [25]: LEEM images of a Rh(110) substrate covered by a submonolayer film of Pd and Au, taken during a water formation reaction in an oxygen–hydrogen mixture at a temperature ≈800 K. The three images were taken at different pressures of the gas mixture.

The interesting point is that by changing the pressure, the near-periodicity of the submicron structures can be modified in a controlled way. This is an example of potential control of microscopic structure geometry via the reaction parameters in catalysis—a class of phenomena with many interesting potential applications.

What is the nature of the different parts of the regular patterns? Spectromicroscopy can provide the answer. We see on the right-hand side of Fig. 12 another LEEM pattern plus three electron-energy-filtered XPEEM images corresponding to three different initial electronic states: Au4f$_{7/2}$, Pd3d$_{3/2}$ and O2p. The result is quite clear: dark (due to high work function) stripes in the LEEM image correspond to oxidized areas whereas the complementary stripes are Au–Pd areas.

The results of Fig. 12 are one case among many of studies of the chemical and geometric features of surface reactions on a microscopic/nanoscopic scale and with high time resolution. They constitute an excellent example of the impact of spectromicroscopy on materials science: not only the microchemical analysis capabilities enhance our understanding of fundamental phenomena but, as seen in Fig. 12, they can reveal new ways to control
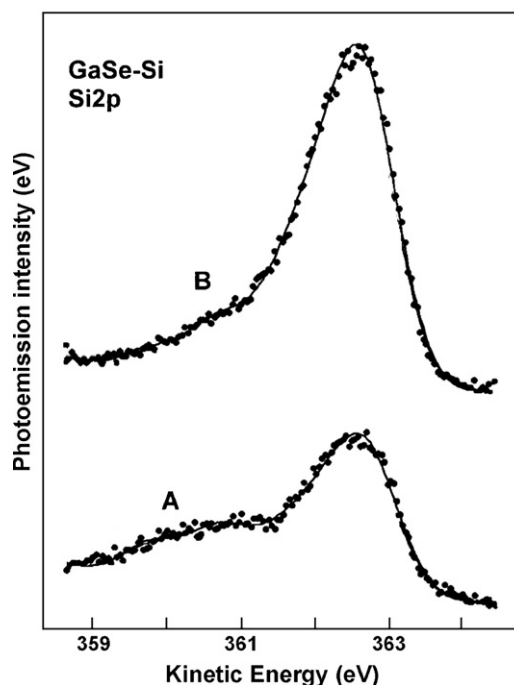
Fig. 11. What causes the band discontinuity fluctuations from point to point? The photoemission spectral lineshapes provide a hint. Here, the Si2p peak changes at different points of a GaSe–Si interface. These modifications reveal different microchemical composition—and suggest that microchemistry is one of the causes of the interface parameter fluctuations. The experimental results were derived from Ref. [21].

microsystems and nanosystems with a great potential for practical applications.

3.2. Complex patterning by diffusion blockage

Figs. 13 and 14 illustrate another nice examples of spectromicroscopy studies of this class of phenomena, performed by spectroscopic SPELEEM at the ELETTRA facility in Trieste. The study concerns a complicated, intriguing and potentially useful set of patterning phenomena on a silicon substrate. The chemical analysis on a microscopic scale enabled Robinson et al. [26] to elucidate the complex nature of the phenomena with a series of elegant experiments. The data discussed here are a representative subset of these results.

The investigated system is a Si(001) substrate covered by a patterned Au overlayer and then by a Ge adlayer. After cleaning and removal of the native oxide, the substrate was covered by a silicon nitride mask with 200 nm × 200 nm openings; then, a 1–2 nm thick Au film was deposited through the mask, followed by 6–8 monolayers of Ge were deposited by molecular beam epitaxy.

Fig. 13 refers to the status after the patterned Au deposition and before the Ge deposition. The top part shows an XPEEM image revealing Au islands and Au-free Si in between them. Local photoemission spectra were taken at the Au sites (dots) and Au-free Si sites (squares): the bottom part of the figure shows two of them.

The spectra concern the Si2p photoemission peak intensity and the difference between the two sites is striking. The Au-free site spectrum simply reveals the peak of bulk silicon. On the contrary, the Au islands reveal two Si features: the bulk peak accompanied by a second one due to oxidized silicon.

These results can be interpreted in terms of a known mechanism [26] whereby Au promotes the oxidation of silicon. In the Au islands, a small Si amount segregates to the surface where it can be oxidized by air. The oxidation is enhanced by the concomitant presence of Au.

We can now move to the second step of the process, Ge deposition. Fig. 14(a) shows a concentration map obtained with energy-filtered XPEEM at an energy corresponding to the Ge3d peak. This picture shows the surface distribution of germanium and reveals that the region corresponding to the original Au sites with oxidized Si now exhibits a low Ge concentration (dark areas). Germanium is instead found in the former Au-free sites.

Fig. 14(b) shows that the silicon (from Si2p results) distribution is quite complementary to that of germanium. One could thus imagine that the Ge pattern is a negative fingerprint of the underlying Au pattern.

Fig. 14(c), however, indicates otherwise. The Au distribution revealed by the Au4f data show only residual presence at the former Au sites and a nonuniform diffusion of Au across the entire region.

These results and several others unveil a number of interesting features. Basically, the absence of Ge from the former Au sites indicates that the silicon oxide nanopatterns are able to block the diffusion of Ge towards such sites. As a result, Ge nucleates more easily in the complementary zones. The Ge, either alone or in combination with Au and Si, appears able to stimulate Au diffusion. The
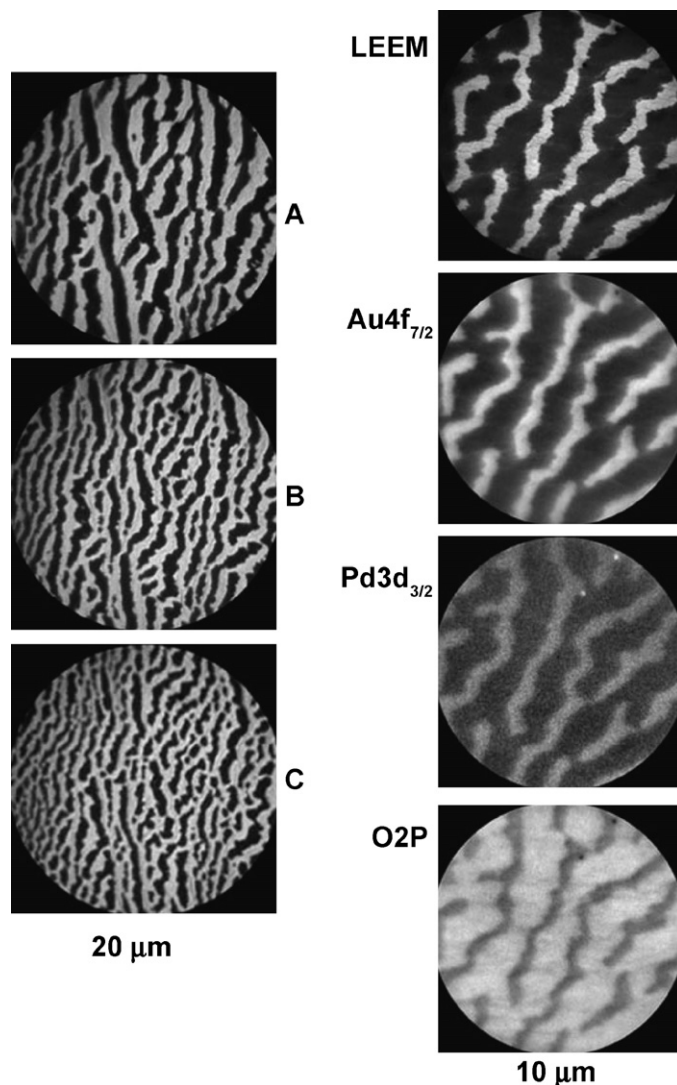

Fig. 12. (Left) 20 μm diameter LEEM pictures of a Rh(110) substrate with a sub-monolayer coverage by Pd–Au, during a ≈800 K water formation reaction in an oxygen–hydrogen mixture. Images A, B and C correspond to three different oxygen–hydrogen pressures: 3.4×10^{-7}, 1.3×10^{-6} and 2.2×10^{-6} mbar. (Right) A 10 μm diameter LEEM picture of the same system and chemical maps of the Au, Pd and O distributions. Data derived from Ref. [25].
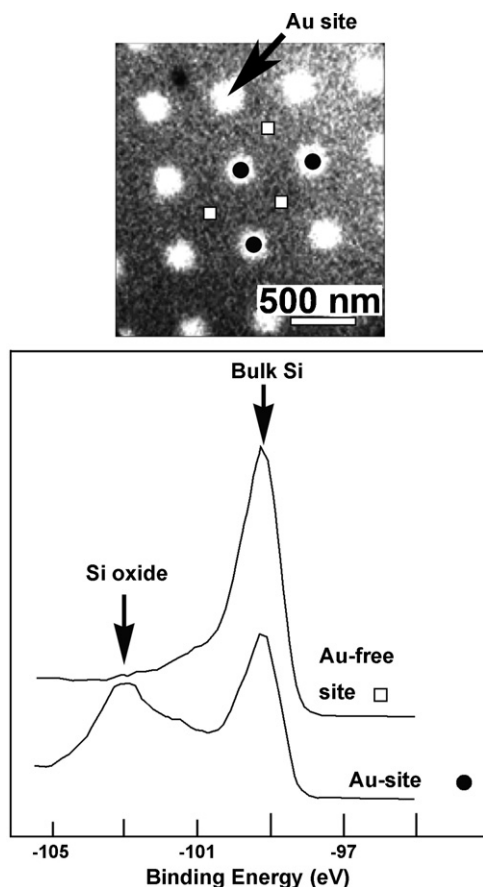
Fig. 13. Results [26] for a Si(001) substrate covered by a patterned Au overlayer and then by a Ge adlayer. The figure illustrates the situation after the patterned deposition of an Au film through a nitride mask, before the Ge deposition. (Top) XPEEM image of Au islands with Au-free Si in between them. (Bottom) two of the local Si2p photoemission spectra taken at Au (dots) and Au-free Si (squares) sites. Results extracted from Ref. [26].

detailed experiments of Ref. [26] reveal many more details about these complex and intriguing mechanisms.

3.3. Nanowires and their transport properties

The previous examples already demonstrated that spectromicroscopy can be quite useful in the study of nanosystems. We would like to discuss here another interesting study that extends beyond microchemistry to measure in a clever way local transport properties.

The experiments, conducted by Kolmakov et al. on Elettra in Trieste [27], first demonstrated that photoelectron spectromicroscopy can at present image and analyze individual quasi-one-dimensional nanosystems. The investigated specimens were SnO_2 nanobelts on a gold support. The results of Fig. 15 were obtained with the Elettra SPEM system.

On the top part of the figure, we see a scanning image produced by photoelectrons originating from the Sn4d core level: the possibility to image an individual microbelt is clearly demonstrated. In addition, the middle and bottom parts of the figure demonstrate microchemical analysis obtained by taking core-level spectra on the tiny quasi-one-dimensional specimen.

The two sets of core-level spectra were taken in the spectral regions of the O1s and Sn3d peaks. Curves (a) were obtained after oxygen plasma treatment and curves (b) after annealing at a temperature of 523 K under ultrahigh vacuum. After best-fitting deconvolution, different peak components can be identified that

reveal some non-trivial microchemical properties. The O1s spectra reflect three species. The first two, SnO and SnO_2, are well correlated with the Sn^{2+} and Sn^{4+} components of the Sn3d spectra. The third O1s component is attributed to chemisorbed oxygen with a series of subspecies and is correlated to the third Sn3d component—that can be explained by Sn chemically bound to the chemisorbed oxygen with a higher coordination than in the dioxide.

Note that the relative spectral weight of the different components changes dramatically between curves (a) and curves (b). For
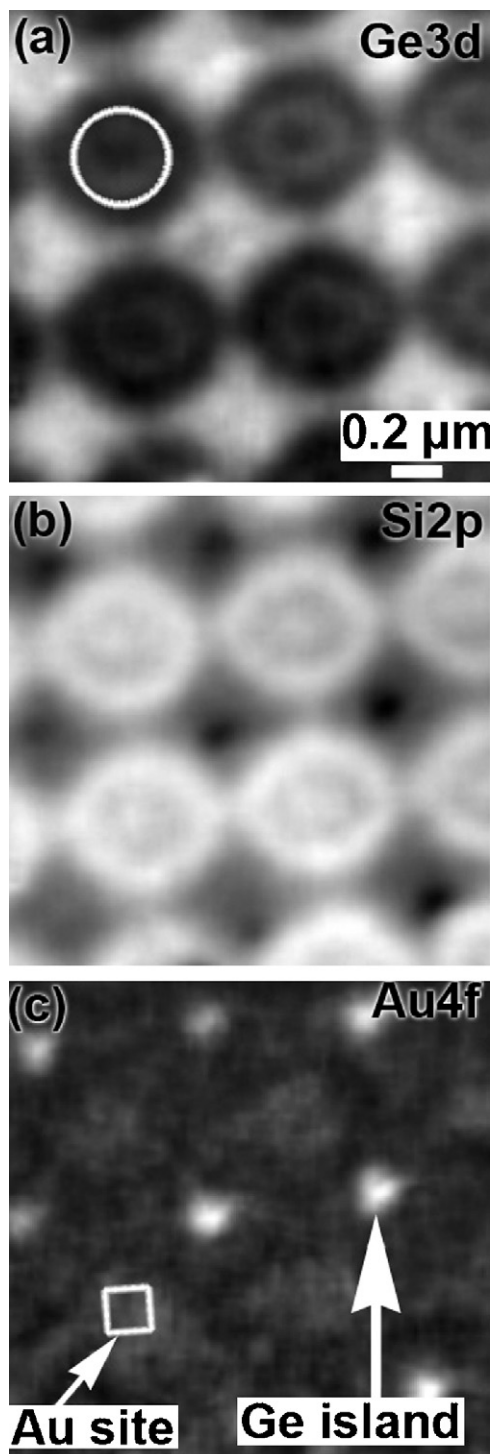

Fig. 14. Images from the same experiment as Fig. 13, taken after Ge deposition. (a–c) XPEEM distribution map of Ge, Si and Au. Results derived from Robinson et al., Ref. [26].
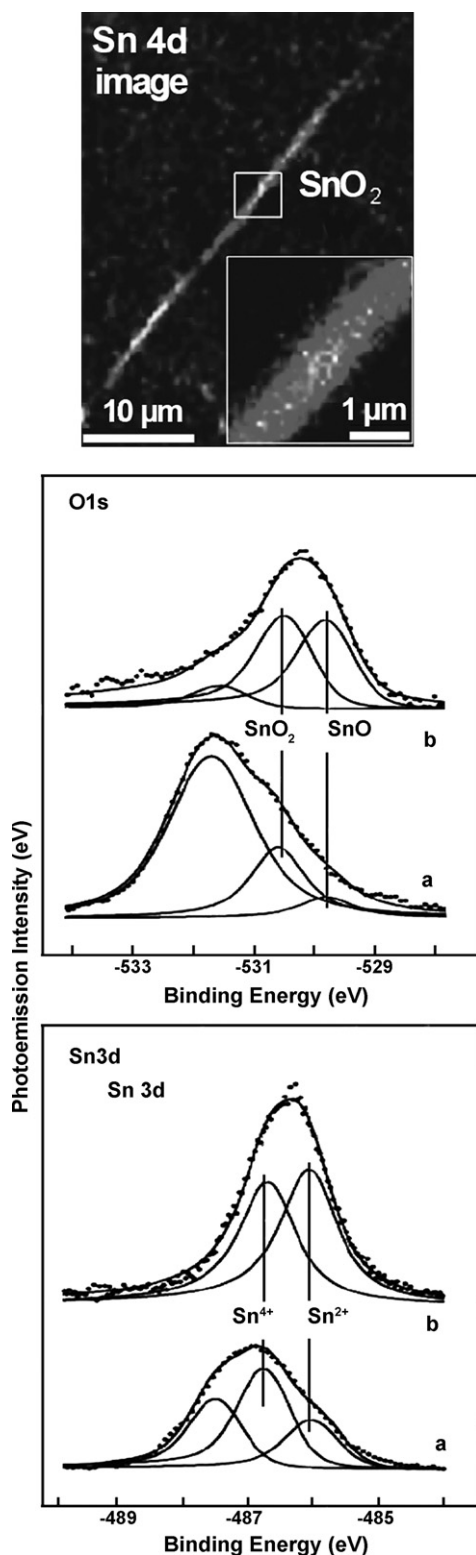
Fig. 15. Spectromicroscopy study of SnO_2 nanobelts on Au. (Top) SPEM image produced by Sn4d photoelectrons, showing an individual microbelt. (Middle and bottom) O1s and Sn3d photoelectron peak from the nanobelt: curves (a) were obtained after oxygen plasma treatment and curves (b) after annealing at a temperature of 523 K under ultrahigh vacuum. The solid lines were obtained by best-fitting deconvolution. Experimental data from Ref. [27].
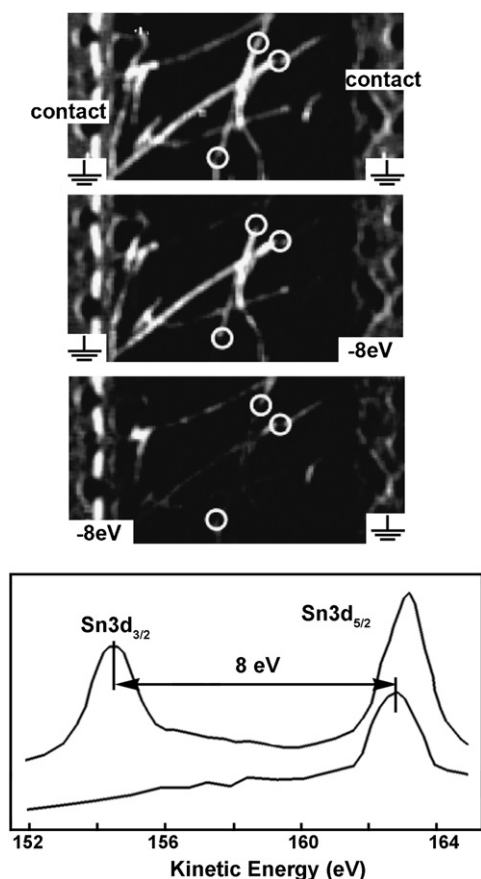

Fig. 16. (Top) spectromicroscopy images of SnO_2 nanowires for three different voltage bias conditions: both contacts at ground (top), left contact at ground and right contact at −8 eV (middle) and vice-versa (bottom). The circles mark highly resistive nodes (junctions between nanowires) that cause some parts of the image to disappear under bias. The mechanism is explained by the bottom part of the figure, showing that the bias shifts the spectra and brings the $Sn3d_{5/2}$ peak outside the energy collection window. Data from Ref. [27].

example, the chemisorbed-oxygen features become much stronger after annealing. This demonstrates once again that spectromicroscopy can perform fine microchemical analysis on nanosystems.

But the analysis, as already mention, can extend beyond microchemistry: an indirect use of photoemission spectroscopy can actually visualize the transport properties of the nanowires. On the top part of Fig. 16 we see spectromicroscopy images of SnO_2 nanowires. These nanosystems are not kept at ground by a conducting substrate but suspended between two contacts.

The three images were obtained detecting photoelectrons originating from the Sn3d electrons. They correspond to different voltage bias conditions: both contacts at ground (top), left contact at ground and right contact at −8 eV (middle) and vice-versa (bottom).

The nanowires are fully observable in the top image but some parts are no longer visible in the two bottom images. What is the cause of this phenomenon? The answer can be found in the bottom part of Fig. 16 that shows spectra for two different bias configuration: both contacts at ground for the top spectrum and one contact at −8 eV for the bottom one. We see that the $Sn3d_{3/2}$ peak shifts by 8 eV between the two curves; the same shift occurs for the $Sn3d_{5/2}$ peak but in the bottom curve it exists the energy collection window—and therefore it can no longer contribute to the image intensity.

If the nanowires had uniform resistance, then the voltage drop between the electrodes would occur steadily along them and the intensity would progressively decrease. This is not the case of the

two bottom images of Fig. 16: some parts are bright and others are dark. This indicates that the resistance is not homogeneous and that the voltage drop is concentrated in certain parts of the nanowires.

A careful analysis can indeed identify some highly resistive nodes (junctions between nanowires), marked by circles in the images. These points keep parts of the nanowires at ground and others biased, influencing the energy position of the photoelectrons and therefore the image intensity.

Thus, the spectromicroscopy images can reveal not only microchemical features but also electrical properties on the nanoscale. The actual analysis is not trivial [27] since the photoemission process itself charges the nanowires and causes rigid shifts of the core-level peaks. However, the general interpretation described above is still valid and in particular the possibility to identify high-resistance points along nanowires. This elegant use of photoemission spectromicroscopy can find many interesting applications.

3.4. Spectromicroscopy of individual nanoparticles

How far can the lateral resolution of photoemission spectromicroscopy go? Practical projections are difficult but one thing is clear: the ultimate limits were not yet reached. And the results are becoming more and more impressive, reaching new dimensions and the corresponding systems in materials science and other domains.

Fig. 17 provides a very nice example: Fraile Rodríguez et al. [28] were able to image and spectrally analyze Co nanoparticles down to the size of 8 nm. Experiments performed with the PEEM technique
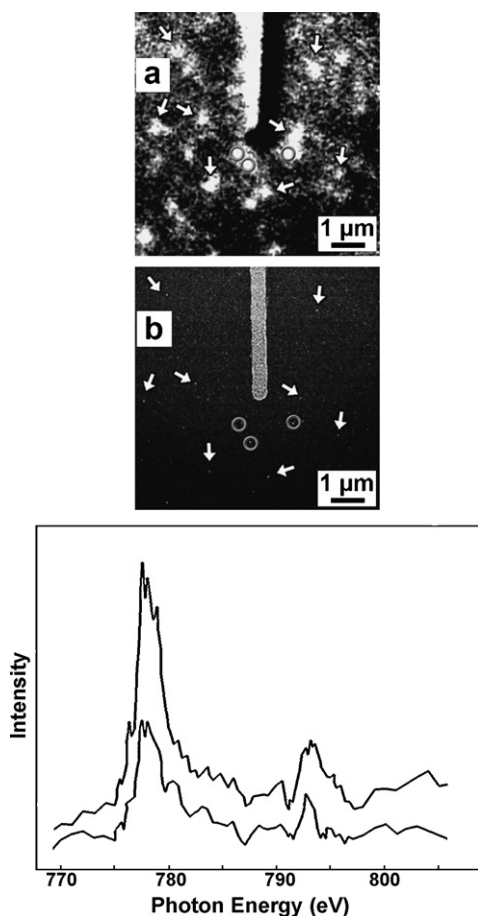

Fig. 17. (a and b) Enhanced PEEM image and SEM image of Co nanoparticles on an Al-covered Si substrate. The processing to obtain image (a) emphasized the Co contributions. (Bottom) PEEM absorption spectra for two individual Co nanoparticles. The experimental results were extracted from Ref. [28].

at the Swiss Light Source (SLS) of the Paul Scherrer Institut (PSI) could also use lithographic marks to correlate the PEEM results with scanning electron microscopy data.

The top and middle parts of Fig. 17 show two images obtained (a) with the PEEM technique, and (b) by scanning electron microscopy (SEM). The imaged system consists of a Si substrate covered first by an Al layer (thickness ≈ 8 nm) and then by Co nanoparticles with average diameter of 8 nm. The PEEM image was obtained by intensifying the Co contribution with the following technique. First, a picture was taken at the photon energy of 778 eV, right above the Co L_3 X-ray absorption edge. Then, a second picture was recorded at 772 eV, below the edge. Afterwards, the first image intensity was pixel-by-pixel divided by the second image. This procedure intensified the cobalt contributions to the processed final picture of Fig. 17.

Fig. 17(a, top) does indeed show features related to the Co nanoparticles, and this conclusion was corroborated by the SEM image of Fig. 17(b). The vertical lithographic marker made it possible to correlate the PEEM and SEM images. The SEM image reveals Co nanoparticles (some of them are marked by arrows) plus groups of 2–3 nanoparticles (marked by circles). The equivalent marking in Fig. 17(a) show the correlation between the features in the two images.

After identifying Co nanoparticles, PEEM (X-ray absorption) spectra were taken for a series of individual nanoparticles by recording as usual the photoemission intensity while scanning the photon energy. The two curves spectra in the bottom part of Fig. 17 are examples of absorption spectra from individual nanoparticles. The spectral structure does correlate well with the near-L_3-edge structure (NEXAFS) of reference Co films. The curves were corrected for small nanoparticle drifts and then divided by the equivalent curves for a region without Co nanoparticles.

In addition to the specific, interesting information provided by these results, their general message is clear. Imaging with photoelectrons is now possible on the scale of a few nanometers. Furthermore, nanochemical analysis is also possible on the same scale.

3.5. Photoelectron spectromicroscopy of artificial kagome spin ice

Magnetic properties on the microscopic and nanoscopic scale constitute one of the most interesting application domains of spectromicroscopy. Such studies greatly profit from the current availability of very intense sources of elliptically polarized synchrotron radiation (e.g., helical undulators) [1,2].

Fig. 18 shows a recent case [29]: the study of spin orientation in artificially constructed blocks of artificial kagome spin ice [30,31]. The top part of the figure shows an example of this highly frustrated system: elongated ferromagnetic islands are arranged on the sites of a kagome lattice forming a honeycomb structure. The top part of Fig. 18 also shows three building blocks of the lattice, consisting of one, two or three combined rings.

There is a general rule (ice rule) [29] that at each vertex there can be either two spins in and one out or, vice-versa, two spins out and one in. This feature and in general the spin orientations of the elements of the lattice can be verified with photoelectron spectromicroscopy.

The experiments were performed by Mengotti et al. [29] at SLS using for elements cobalt and permalloy (80% Ni + 20% Fe) islands patterned on silicon with lithography methods and then capped with Al to prevent oxidation. The bottom part of Fig. 18 shows PEEM images of three lattice building blocks formed by such elements, together with schemes explaining the interpretation of these images. The pictures were obtained with photon energies near the Co L_3 edge, using circularly polarized X-rays and exploiting the X-ray magnetic circular dichroism (XMCD) effect.
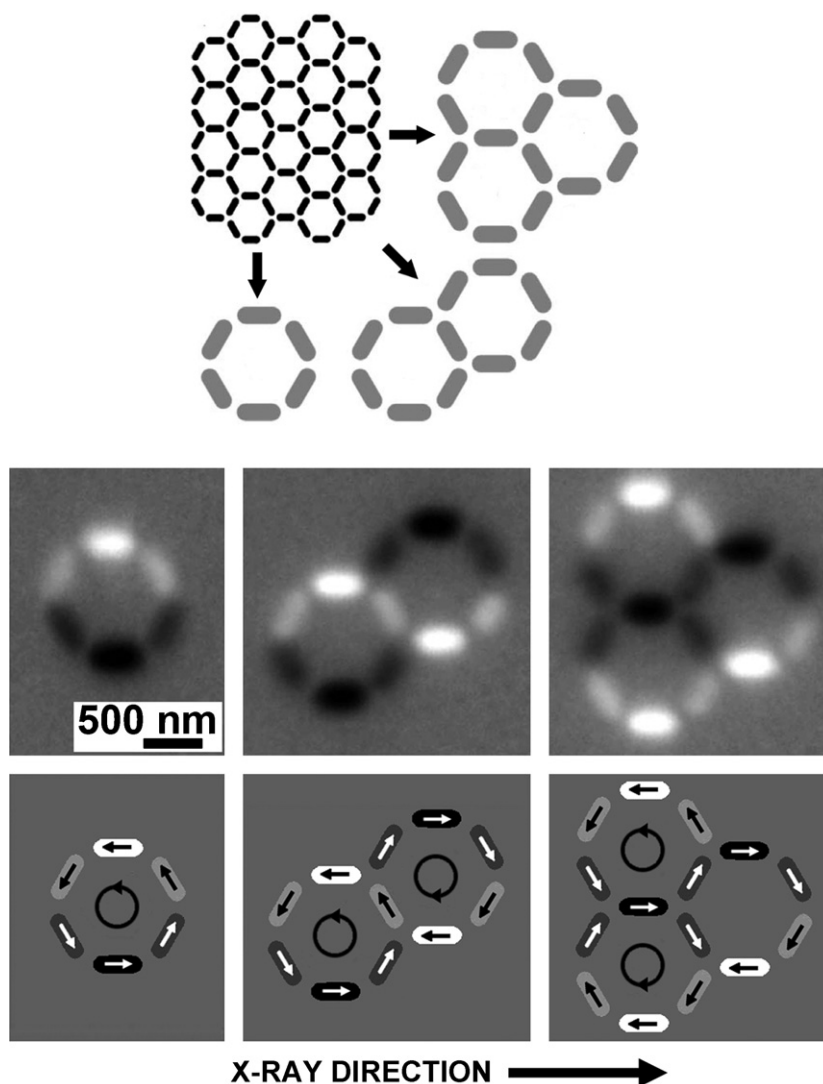
Fig. 18. (Top) Scheme of a Kagome spin ice system; the picture also shows three different building blocks. (Bottom) PEEM images of an artificial Kagome spin ice lattice whose elements are cobalt and permalloy (80% Ni + 20% Fe) islands patterned on silicon and then capped with Al. Also shown are schemes explaining the interpretation of these images. The pictures were obtained with photon energies near the Co L_3 edge, using circularly polarized X-rays and exploiting the X-ray magnetic circular dichroism (XMCD) effect. Data derived from Ref. [29].

The XMCD phenomenon modifies the intensity of the absorption as the angle between the magnetic moment orientation of the specimen and the X-ray circular polarization vector changes. In such a way, the image intensity becomes a probe of the magnetic moment orientation. We see indeed in the images different intensities for different components. However, the intensity does not change within a given element, indicating that the elements are magnetic monodomains with all the spins oriented in the same direction.

The schemes in the bottom part of Fig. 18 show the spin orientations derived from the intensities and the agreement with the above-mentioned vertex rule. This approach makes it possible to study spin orientations on the nanoscale in a rather straightforward way. As such, it is an exceedingly powerful probe for the investigation of magnetic issues on the nanoscale.

3.6. Spectromicroscopy with the SPHINX instrument: biology and materials science

The recent technological evolution of photoemission spectromicroscopy made it possible to reach unprecedented performances. One significant example of this progress is the instrument SPHINX (spectromicroscope for the photoelectron imaging of nanostructures with X-rays) developed by P.U.P.A. Gilbert (G. De Stasio) and co-workers [32] at the Wisconsin Synchrotron Radiation Center in Stoughton. Fig. 19 shows the electron optical layout of the system, which is based on the ELMITEC XPEEM module (including six magnetic lenses: objective, transfer, field, intermediate and two projective elements)—with the addition of two stigmators and five deflectors to correct for the misalignments of magnetic lenses and achieve accurate focusing.

In general terms, the spatial resolution of a PEEM-class instrument [32] is affected by the spherical and chromatic aberrations of the objective lens. The chromatic aberrations play a key role and depend on the energy spectrum of the electrons. Such aberrations are minimal when the exciting photon energy is in the ultraviolet range since the electrons have very low energy. The problem is more severe for photoelectrons produced by X-rays whose energy spread is broad. This problem can be alleviated by an aperture placed at the back focal plane of the objective lens that filters out fast electrons—but at the price of reduced flux.
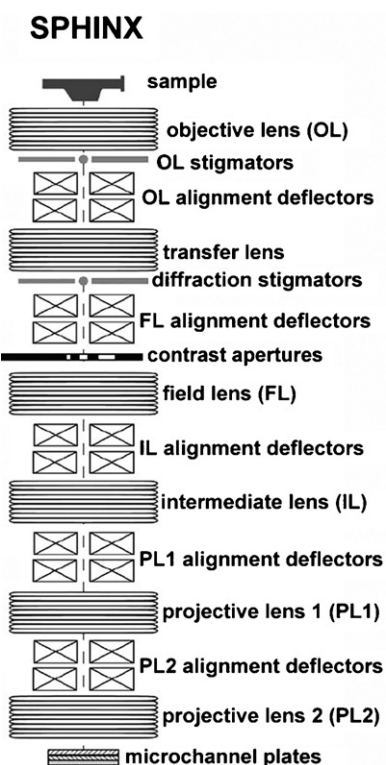
SPHINX

Fig. 19. Scheme of the electron optical system of SPHINX (spectromicroscope for the photoelectron imaging of nanostructures with X-rays) developed by P.U.P.A. Gilbert (G. De Stasio) and co-workers [32] at the Wisconsin Synchrotron Radiation Center in Stoughton. Drawing adapted from Ref. [32].

Experimental tests on SPHINX [32] demonstrated a Rayleigh-criterion resolution below 10 nm with monochromatic X-rays. These performances make it possible to routinely image, for example, nanoparticles with size of a few ten nanometers—and are quite close to the theoretical resolution limit ≈5 nm. Fig. 20 shows images of individual lead nanoislands on silicon demonstrating once again, like Fig. 17, the power of advanced spectromicroscopes in analyzing nanosystems.

Fig. 21 shows an example of microchemical analysis applied to a biological specimen. The top part is a PEEM image acquired with SPHINX using 1.2 keV photons of human glioblastoma cells grown on a silicon substrate. Individual cells and their details are clearly visible. The bottom part is a chemical map showing the specific distribution of phosphorus. The map was obtained by taking images at 139 and 135 eV photon energies; the first one corresponds to a peak in the P2p absorption threshold and the other is off-peak. The distribution map of the bottom part of Fig. 21 was then obtained by dividing pixel-by-pixel the first image by the second.

The chemical map clearly and convincingly shows the P-rich areas of the cell nuclei. This is an example of the many present applications of spectromicroscopy to microchemical analysis at the cellular and subcellular level.

Fig. 22 illustrates at the same time a novel and interesting application of spectromicroscopy to the life sciences and a new technique to analyze the orientation of microcrystals and nanocrystals [33]. The investigated system is nacre from red abalone. Nacre is a composite material formed by aragonite ($CaCO_3$) tablets and organic layers; besides its biological interest, it is also quite technologically intriguing because its structure results in excellent strength and toughness. Indeed, nacre is formed primarily (95%) by aragonite but it s 3000 times tougher than aragonite itself!

The figure shows a PEEM image of a polished section of red abalone shell. The tablets are clearly visible but, in addition, the image also reveals that the aragonite crystals orientation is not the same for different tablets. This result was obtained using the PEEM technique known as PIC (polarization-dependent imaging contrast) [33].

The image of Fig. 22 was obtained by first taking micrographs with the photon energies 534 and 518 eV. The first energy corresponds to the oxygen π^* absorption edge in aragonite whereas the second is below the edge. The processed image of Fig. 22 was then obtained by pixel-by-pixel dividing the edge picture by the pre-edge picture. The intensity is thus clearly related to oxygen in aragonite.

In addition, the absorption intensity depends on the orientation of the X-ray polarization vector (note that synchrotron radiation is polarized [1,2]) with respect to the crystal *c*-axis. This explains the intensity differences between different tablets in Fig. 22: they are due to different crystal orientations.

Results of this kind are very valuable: P.U.P.A. Glbert (G. De Stasio) et al. [33] used them to shed new light on the remarkable properties of red abalone nacre. They specifically revealed the complex interplay between crystal orientation, microchemistry and other factors that were so far largely ignored due to the lack of adequate experimental probes.

This concludes our short series of examples of the current status, performances and applications of different kinds of photoemission spectromicroscopy and spectronanoscoy. Many more results of other authors and institutions could be presented but the set discussed above already provides a clear illustration of the rapid technological progress in this domain and of the fast expansion of its scope.
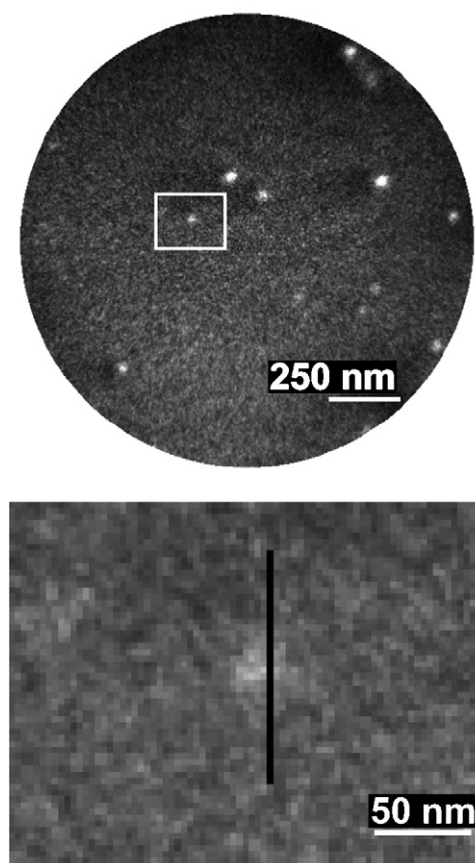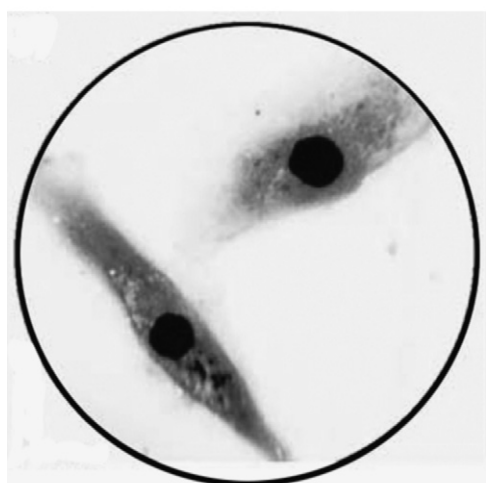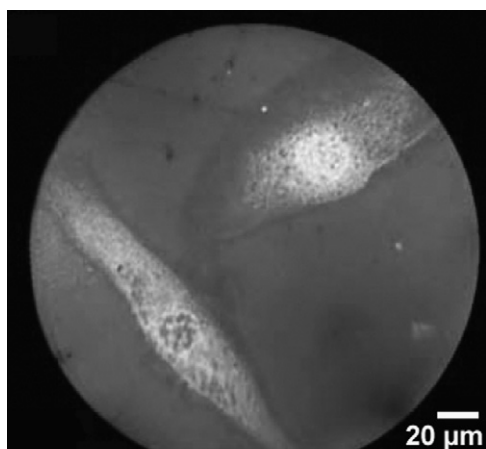

Fig. 20. Two SPHINX images showing individual Pb nanoislands on a silicon substrate, derived from Ref. [32].

Fig. 21. (Top) PEEM image of human glioblastoma cells on silicon substrate acquired with the SPHINX system using 1.2 keV photons. (Bottom) Chemical phosphorus distribution map; the image processing steps are described in the text. Data extracted from Ref. [32].

3.7. PEEM applications in biotechnology

The combination of chemical analysis and high lateral resolution makes photoemission spectromicroscopy and spectronanoscopy particular attractive for experiments relevant to biotechnology.
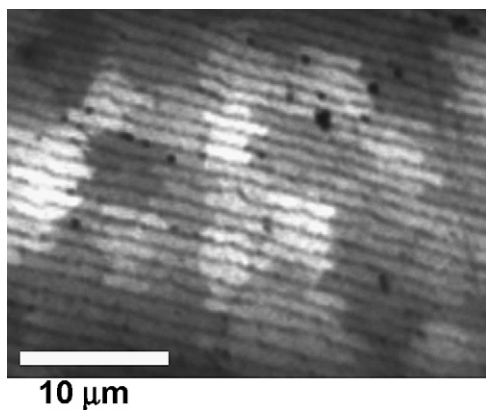

Fig. 22. Red abalone nacre oxygen distribution map obtained with the PEEM technique known as PIC (polarization-dependent imaging contrast) [33]—that reveals the local crystal orientation of individual tablets from the image intensity. Data derived from Ref. [33].
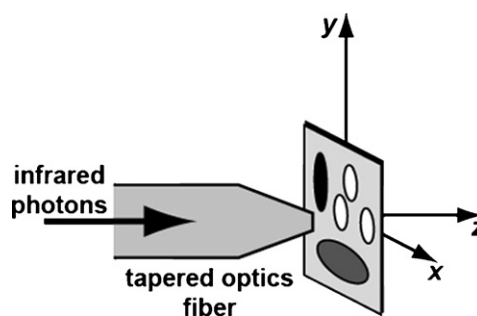

Fig. 23. Schematic explanation of how near-field microscopy beat the diffraction limits: see the text for the details.

One nice example is provided by the XPEEM experiments of A. P. Hitckcock's laboratory [34] on the distribution of human serum albumine (HSA) on candidate biomaterial substrates. This was a reference study since HSA, the most abundant of plasma proteins, is commonly used as a model case to investigate protein–surface interactions.

The results of Ref. [34] clearly demonstrated the usefulness, power and versatility of spectromicroscopy and spectronanoscopy in biotechnology. The data revealed the differences between the absorption on polystyrene and polymethylmethacrylate as a function of the acidity—and the special absorption effectiveness of the interface between the two domains. The results also elucidated the links between absorption, protein surface charge and protein surface structure. In general terms, they demonstrated that the laterally resolved versions of photoemission techniques can now tackle complex nanochemical problems in bioengineering systems.

4. Other sides of synchrotron spectromicroscopy: near-field infrared techniques

This review is focused on one class of synchrotron spectromicroscopy techniques: those based on photoemission. However, synchrotron and free electron laser [1,2] sources are used for many other techniques that combine spectroscopic performances with high spatial resolution [2]. We note, for example, the fluorescence microprobe and micro-EXAFS or micro-XANES with focused X-ray beams [2].

In a different spectral range, free electron lasers enabled the implementation of near-field infrared microscopy in its "spectroscopic" mode, revealing individual vibrational modes and therefore the corresponding chemical species on a microscopic scale [36–38].

The principle of near-field microscopy [39] is schematically illustrated in Fig. 23. A tapered optics fiber is placed very close to a specimen and brings light into it from its small aperture. The coordinate system xyz has its origin at the specimen surface.

First, let us assume that the specimen is imaged with a conventional microscope whose optical system is placed far from the specimen. This is a "far-field" configuration rather than a near-field geometry like that created in Fig. 23 by the proximity of the fiber to the specimen. We will call $\boldsymbol{k}$ the photon k-vector, with components k_x, k_y, and k_z.

The uncertainty principle requires that $\Delta x > 2\pi/\Delta k_x$; on the other hand, Δk_x cannot be larger than $|k_x| = (|k_x|^2 - k_y^2 - k_z^2)^{1/2} = \left(\left((2\pi/\lambda)^2 - k_y^2 - k_z^2\right)^{1/2}\right)^{1/2}$ — and therefore is smaller than $2\pi/\lambda$, where λ is the wavelength. Thus:

$$\Delta x > \lambda \tag{2}$$

This and the equivalent relation for Δy is the well-known "diffraction limit" [2] for the spatial resolution of far-field microscopy. Note

that this is not a technological limit but a fundamental feature of optics.

Can the diffraction limit be beaten? The answer is positive and the key is a near-field configuration like that of Fig. 23. Photons can be brought to a small spot on the sample by the tapered fiber and images can be obtained by scanning the fiber tip with respect to the sample while detecting the reflection or the absorption of the photons.

Why can this approach beat the diffraction limit? The answer is simple: the above conclusion that $(((2\pi/\lambda)^2 - k_y^2 - k_z^2)^{1/2})^{1/2}$ is smaller than $2\pi/\lambda$ is only valid if both k_y and k_z are real quantities. Now, k_z is real if the photon wave propagates along the z-direction—but it becomes imaginary if it is absorbed by the specimen or, in general, if it is an evanescent wave. In this case Δx and Δy can be smaller than λ, beating the diffraction limit.

Practically speaking, obtaining high lateral resolution with this scanning near-field optical microscopy (SNOM) approach requires putting the fiber tips very close to the sample surface. The bonus is that the device can also operate as a scanning atomic force microscope (AFM) [35]. This is important since one can thus correlate microchemical properties revealed by SNOM and the specimen micromorphology.

Several other technical conditions exist for the practical implementation of SNOM. One of the most critical is the preparation of highly efficient tapered fibers to guarantee a sufficient photon flux and a good signal level. This is the main motivation for using a free electron laser source when SNOM is extended from visible photon energies to the infrared (IR) [35].

The diffraction limit is actually more severe for IR microscopy than for visible microscopy because of the larger wavelengths. Therefore, using a SNOM approach is quite an attractive possibility. Obtaining SNOM images in the infrared is not extremely difficult, but implementing the spectromicroscopic mode of IR SNOM is a challenging task because of the low signal level. This problem is solved by a high-brightness free electron laser source [35].

IR SNOM spectromicroscopy can provide fine chemical information on a microscopic scale primarily by detecting vibrational absorptions [35]. These are due to quantum transitions between the energy levels of the normal modes of the system. Such levels are related to the chemical species and therefore can be used to detect them. However, this attractive opportunity opened in principle by IR SNOM cold not be implemented in practice until Cricenti and co-workers [35] started using the very bright infrared source of the Vanderbilt University Free Electron Laser.

Figs. 24 and 25 show two of the many examples of results of this spectromicroscopy approach. In Fig. 24, the top and middle parts are reflectivity IR SNOM images of a keratinocyte cell (HaCaT line) on a glass cover slide [35]. The two images were taken with IR beams of wavelength 6.95 and 6.1 nm, corresponding to the sulphide stretch vibrational absorption (primarily from the cell growth medium) and to the amide I absorption band related to the C=O bond stretch. The images reveal thus the spatial distribution of such modes and of the corresponding chemical components, confirming the spectromicroscopic capabilities of IR SNOM when a free electron laser provides sufficient IR intensity.

The bottom part of Fig. 24 is a reflectivity scan along the line A–B of the 6.1 μm image. The purpose of this scan is to evaluate the spatial resolution and demonstrate that it goes beyond the diffraction limit. Indeed, the scan indicates a resolution of the order of 100 nm, therefore of the order of $\lambda/60$.

Fig. 25 shows an example [38] of spectromicroscopic IR SNOM performed in absorption. The specimen was a glass supported DOPC (1,2-dioleoyl-sn-glycero-3-phoshocoline) lipid membrane. The bottom curve is a Fourier transform infrared (FTIR) spectrum revealing different vibrational modes: antisymmetric stretch of the
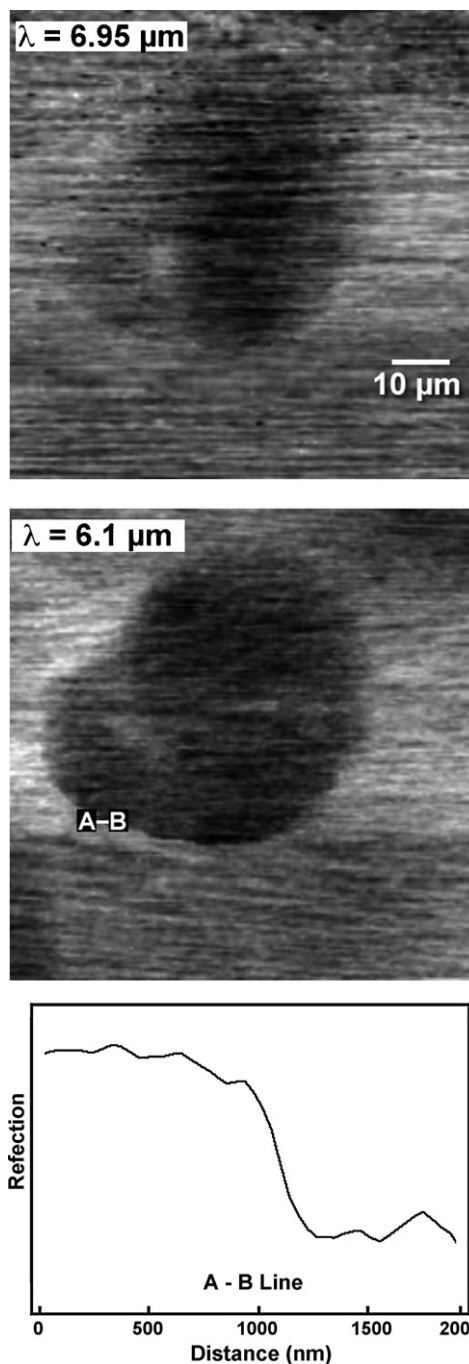

Fig. 24. (Top and middle) reflectivity IR SNOM images of a keratinocyte cell (HaCaT line) on a glass cover slide [35]. The images were taken with the IR wavelength 6.95 and 6.1 nm, corresponding to the sulphide stretch vibrational absorption and to the amide I absorption band related to the C=O bond stretch. (Bottom) reflectivity scan along the line A–B of the 6.1 μm image, demonstrating a spatial resolution $\approx$100 nm $\approx \lambda/60$, well beyond the diffraction limit. Data extracted from Ref. [35].

$(PO_2)^-$ group (8.0 μm wavelength), C=O stretch (5.75 μm) and the CH_2 scissoring mode (6.8 μm).

IR SNOM absorption maps were taken for each of these wavelengths and are shown in the upper part of the figure. There are clear similarities between these images, as it should be expected. On the contrary, the image for 6.1 μm (no vibrational absorption band) exhibits no structure. This demonstrates, in particular, that the features in the other figures are not topographical artifacts.

The potential applications of spectromicroscopic IR SNOM are very broad and largely complementary to other types of spectromi-

croscopy. This technique is thus a valuable addition to the growing arsenal of microchemistry tools using accelerator-based photon sources in different spectral ranges.

5. Information content and data taking strategies

The use of spectromicroscopy instead of mere spectroscopy raises some interesting questions about the optimization of the data taking strategy [40,41]. The basic problem already exists for spectroscopy and can be formulated in the following way [40]. The energy resolution of the spectroscopy data must be optimized taking into account the specific objective of the experiment. For example, if we want to distinguish between two chemical states of a given element in the system, we can take core-level peak spectra and detect their energy difference. Up to a certain point, by increasing the resolution we obtain more information. However, when we use more resolution that it is needed we waste valuable synchrotron beamtime. This has an impact on the cost of research since the effective value of one hour of beamtime can exceed 10^3 euros.

The problem is much more serious [40] for spectromicroscopy than for spectroscopy since the techniques operate in three dimensions rather than one: energy and two spatial directions. For example, a similarly excessive resolution for two parameters increases the waste of beamtime (and money) quadratically. If more parameters are involved such as polarization vectors or photoelectron emission directions, the situation can become catastrophic.

The analysis of the information optimization becomes increasingly complex with the number of parameters [40]. With only one parameter, e.g., energy in standard spectroscopy, the treatment based on the information entropy is quite straightforward. And the result matches intuition: for example, when taking a Gaussian-shaped peak the best strategy is to use a resolution equal to the linewidth—rather than overkilling the problem with excessive resolution. This conclusion is derived [40] from the problem of the "maximum extractable information" that takes into account both the resolution and the signal-to-noise level but requires the *a priori* knowledge of the mathematical lineshape.

With more parameters, e.g., in spectromicroscopy, the mathematical optimization based on the information entropy is more complex [40]. A comprehensive analysis leads to five "common

sense rules" [41] that are based on a rigorous theoretical background:

First of all, the specific objectives of the experiments must be well defined before the data taking starts. This is required to analyze the optimal resolution levels and avoid unnecessary waste.

Generally speaking, if each parameter is analyzed independent of the others the maximum extractable information analysis always leads to an optimal resolution similar to the width of the (energy or spatial) features that one tries to detect. For example, to determine the position of a dot of a given diameter, the spatial resolution should be similar to the diameter.

Each mode of spectromicroscopy has its own rules for the optimization of the data taking strategy. Rules of one mode cannot be automatically transferred to others without first checking the theoretical background.

Errors in planning the data taking strategy that result in excessive resolution levels can lead to disastrous waste of beamtime and money and therefore must be avoided if at all possible.

Common sense data taking planning based on intuition can work in some cases but in others it can lead to serious mistakes. A careful mathematical analysis of each case is preferable—but sometimes it leads to unsolvable problems.

On the light of the above discussion, the spectacular increase in the flux and brightness of synchrotron sources has a financial impact. The decrease in the data taking time also decreases the cost of the experiment. This effect often goes unnoticed, but with a large number of experiments its impact is not negligible.

Contrary to the past, even the most advanced synchrotron-based techniques like spectromicroscopy are effectively open to a broad spectrum of users independent of their own resources, with access primarily based on merit. This "democratic" phenomenon, as many other politically positive evolutions, is also a result of the cost decrease. In this sense synchrotron beamtime has the same "social" phenomenology of standard commodities like food.

6. The future: more than just better sources

The progress of synchrotron sources started more than forty years ago and, amazingly, is still accelerating [1,2]. The nest big step will be the commissioning of X-ray free electron lasers with their unprecedented peak brightness and short pulse duration. The impact on spectromicroscopy will certainly be quite important.

Photon sources, however, are not the only factor in the progress of spectromicroscopy. Other instrumentation advances played an important role all along the development of this subdomain. It is safe to predict that they will continue to do so in the future. For example, improvements in the detector efficiency are highly desirable. And the use of free electron lasers with their peak brightness will require optics systems resistant to photon damage and can cause space charging and sample deterioration problems.

We would like to discuss here in some detail a specific example of important instrumentation improvements: the progress in focusing devices for X-rays. The advances of these past two years were rather spectacular [42] thanks to a number of new technological approaches.

Fig. 26 shows, for example [42], results of the optimization of Fresnel zone plates (FZP) for hard-X-rays. The two top images (a) and (b) were taken with scanning electron microscopy with different magnifications and show different parts of the FZP, consisting of an Au pattern over a 1 μm thick silicon nitride membrane. The membrane and the pattern were fabricated with a combination of advanced techniques including low-pressure chemical vapor deposition, electron beam writing, lithography processing and electrodeposition.
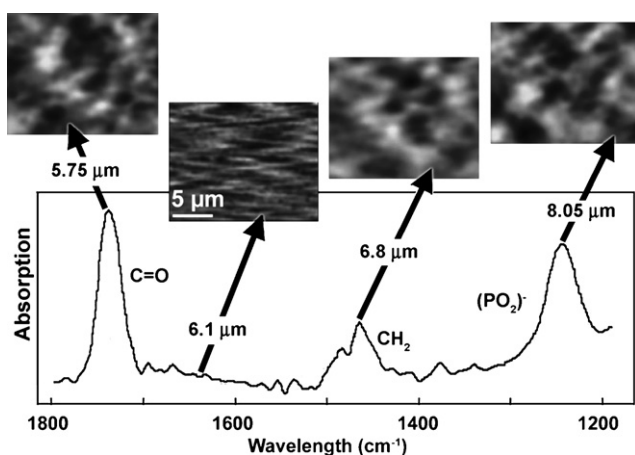

Fig. 25. (Bottom) FTIR spectrum of a DOPC (1,2-dioleoyl-sn-glycero-3-phoshocoline) lipid membrane, revealing different vibrational modes: antisymmetric stretch of the $(PO_2)^-$ group (8.0 μm wavelength), C=O stretch (5.75 μm) and the CH_2 scissoring mode (6.8 μm). The top part shows IR SNOM images corresponding to these three wavelength, plus the image for 6.1 μm that does no correspond to an absorption band. Results extracted from Ref. [38].
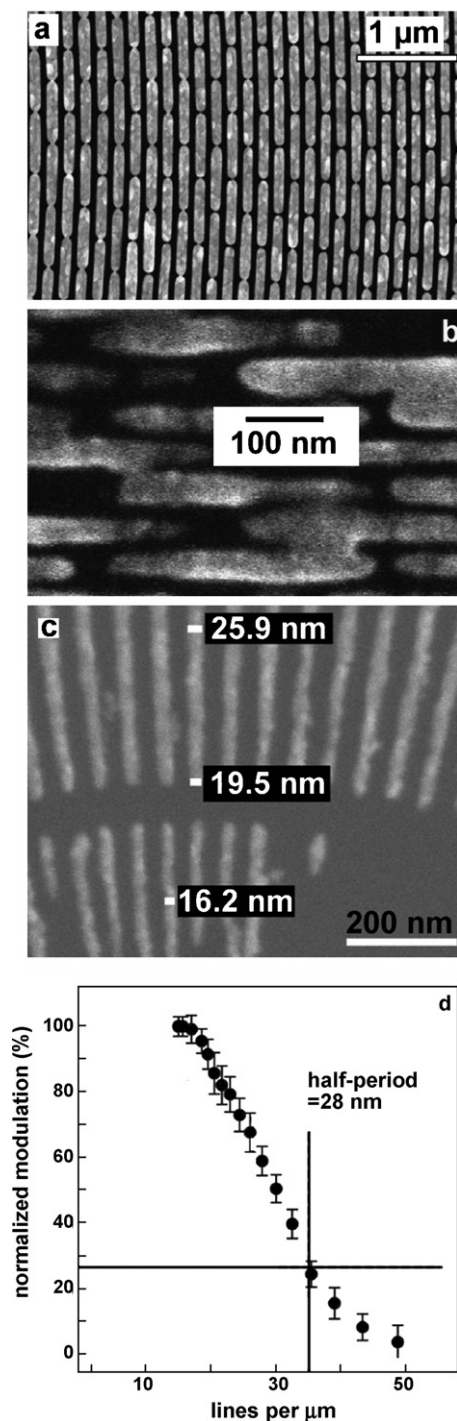
Fig. 26. (a and b) Scanning electron micrographs of the advanced Fresnel zone plate (FZP) for hard-X-rays described in Ref. [42]. (c) Optical micrograph obtained with this FZP: the smallest visible features sizes are 16–17 nm. (d) Modulation transfer function (MTF) test demonstrating a Rayleigh resolution of 29 nm. Results derived from Ref. [42].

In order to work effectively in the hard-X-ray range (>8 keV photon energy), the Au pattern must be quite thick and the aspect ratio correspondingly large. In the case of Fig. 26, the thickness was 450 nm, the width of the outermost (narrowest) FZP zone 30 nm, giving an aspect ration of 15. Reaching such an aspect ratio while maintaining mechanical stability was a major nanofabrication challenge [42].

Fig. 26c shows an optical micrograph obtained with the FZP: the smallest features in the test pattern are as narrow as 16–17 nm. This

suggest a spatial resolution <30 nm. The conclusion was corroborated by more rigorous tests [42] including measurements of the modulation transfer function (MTF) and power spectrum analysis. An example of MTF results is shown in the bottom part of Fig. 26: the data indicate a Rayleigh resolution of 29 nm. Overall, the tests confirm that the 30 nm resolution level was successfully passed.

These results are an example of the impressive technological developments that are making the different types of photoelectron spectromicroscopy techniques – as well as synchrotron and free electron laser spectromicroscopy in general – increasingly powerful. The widespreading applications of these new instruments certainly have, as the title of this review indicated, a growing impact on materials science and the life sciences.

Acknowledgments

References

[1] G. Margaritondo, Introduction to Synchrotron Radiation, Oxford, New York, 1988.
[2] G. Margaritondo, Elements of Synchrotron Light for Biology, Chemistry, and Medical Research, Oxford, New York, 2002.
[3] G. Margaritondo, J. Synchrotron Radiat. 2 (1995) 148–154.
[4] G. Margaritondo, F. Cerrina, Nuclear Instrum. Methods A191 (1990) 26–35.
[5] D.W. Turner, I.R. Plummer, H.Q. Porter, Philos. Trans. R. Soc. Lond. A318 (1986) 219–241.
[6] B.P. Tonner, G.R. Harp, Rev. Sci. Instrum. 59 (1988) 853.
[7] C. Capasso, W. Ng, A.K. Ray-Chaudhuri, S.H. Liang, R.K. Cole, Z.Y. Guo, J. Wallace, F. Cerrina, J. Underwood, R. Perera, J. Kortright, G. De Stasio, G. Margaritondo, Surf. Sci. 287–288 (1993) 1046–1050 (and the earlier references therein).
[8] J. Voss, H. Dadras, C. Kunz, A. Moewes, G. Roy, H. Sievers, I. Storjohann, H. Wongel, J. X-Ray Sci. Technol. 3 (1992) 85–108.
[9] H. Ade, J. Kirz, H. Rarback, S. Hulbert, E. Johnson, D. Kern, P. Chang, Y. Vladimirsky, in: D. Sayre, M. Howells, J. Kirz, H. Rarback (Eds.), X-Ray Microscopy II, Springer, New York, 1987, p. 280.
[10] P.L. King, R. Browning, P. Pianetta, I. Lindau, M. Keenlyside, G. Knapp, Phys. Scripta 41 (1990) 413–417.
[11] S. Anders, H.A. Padmore, R.M. Duate, T. Renner, T. Stammler, A. Scholl, M. Scheinfein, J. Stöhr, Rev. Sci. Instrum. 70 (1999) 3973–3981.
[12] R. Nyholm, M. Eriksson, K. Hansen, O.-P. Sairanen, S. Werin, A. Flodström, C. Törnevik, T. Meinander, M. Sarakontu, Rev. Sci. Instrum. 60 (1989) 2168–2171.
[13] W. Gudat, C. Kunz, Phys. Rev. Lett. 29 (1972) 169–172.
[14] A. Locatelli, E. Bauer, J. Phys. C20 (2008) 093002.
[15] C. Capasso, A.K. Ray-Chaudhuri, W. Ng, S.H. Liang, R.K. Cole, J. Wallace, F. Cerrina, G. Margaritondo, J. Underwood, J. Kortright, R. Perera, J. Vac. Sci. Technol. A9 (87–288) (1991) 1248–1253.
[16] W. Ng, A.K. Ray-Chaudhuri, S.H. Liang, S. Singh, H. Solak, J. Welnak, F. Cerrina, G. Margaritondo, J. Underwood, R. Perera, J. Kortright, Nuclear Instrum. Methods A347 (1994) 422–430.
[17] G. De Stasio, D. Dunham, B.P. Tonner, D. Mercanti, M.T. Ciotti, P. Perfetti, G. Margaritondo, J. Synchrotron Radiat. 2 (1955) 106–112.
[18] F. Cerrina, A.K. Ray-Chaudhuri, W. Ng, S.H. Liang, S. Singh, J. Welnak, J. Wallace, C. Capasso, J. Underwood, J. Kortright, R. Perera, G. Margaritondo, Appl. Phys. Lett. 83 (1993) 63–65.
[19] F. Gozzo, M. Marsi, H. Berger, G. Margaritondo, A. Ottolenghi, A.K. Ray-Chaudhuri, W. Ng, S.H. Liang, S. Singh, J. Welnak, J. Wallace, C. Capasso, F. Cerrina, Phys. Rev. B48 (1993) 17163–17167.
[20] F. Gozzo, P. Berger, I.R. Collins, G. Margaritondo, W. Ng, A.K. Ray-Chaudhuri, S.H. Liang, S. Singh, F. Cerrina, Phys. Rev. B51 (1995) 5024–5028.
[21] M. Zacchigna, L. Sirigu, J. Almeida, H. Berger, L. Gregoratti, M. Marsi, M. Kiskinova, G. Margaritondo, Appl. Phys. Lett. 73 (1998) 1859–1861.
[22] F. Capasso, G. Margaritondo, Heterojunction Band Discontinuities: Physics and Device Applications, North-Holland, Amsterdam, 1987.
[23] G. Margaritondo, C. Capasso, F. Patella, C. Quaresima, A. Savoia, F. Sette, J. Vac. Sci. Technol. A2 (1984) 508–510.
[24] G. Margaritondo, J.E. Rowe, S.B. Christman, Phys. Rev. B14 (1976) 5396–5403.
[25] A. Locatelli, M. Kiskinova, Chem. Eur. J. 12 (2006) 8890–8896.
[26] J.T. Robinson, F. Ratto, O. Moutanabbir, S. Heun, A. Locatelli, T. Onur Mentes, L. Aballe, O.D. Dubon, Nano Lett. 7 (2007) 2655–2659.

[27] A. Kolmakov, S. Potluri, A. Barinov, T.O. Mentes, L. Gregoratti, M.A. Niño, A. Locatelli, M. Kiskinova, ACS Nano 2 (2008) 1993–2000.
[28] A. Fraile Rodríguez, F. Nolting, J. Bansmann, A. Kleibert, L.J. Heyderman, J. Magnetism Magnetic Mater. 316 (2007) 426–428.
[29] E. Mengotti, L.J. Heyderman, A. Fraile Rodríguez, A. Bisig, L. Le Guyader, F. Nolting, H.B. Braun, Phys. Rev. B78 (2008) 144402.
[30] G. Möller, R. Moessner, Phys. Rev. Lett. (2006) 237202.
[31] A.S. Wills, R. Ballou, C. Lacroix, Phys. Rev. B66 (2002) 144407.
[32] B. Frazer, M. Girasole, M. Wiese, T. Franz, G. De Stasio, Ultramicroscopy 99 (2004) 87–94.
[33] P.U.P.A. Gilbert, R.A. Metzler, D. Zhou, A. Scholl, A. Doran, A. Young, M. Kunz, N. Tamura, S.N. Coppersmith, J. Am. Chem. Soc. 130 (2008) 17519–17527.
[34] L. Li, A.P. Hitchcock, R. Cornelius, J.L. Brash, A. Scholl, A. Doran, J. Phys. Chem. B 112 (2008) 2150–2158 (and the references therein).
[35] D. Vobornik, G. Margaritondo, J.S. Sanghera, P. Thelen, I.D. Aggarwal, B. Ivanov, N.H. Tolk, V. Manni, S. Grimaldi, A. Lisi, S. Rieti, D.W. Piston, R. Generosi, M. Luce, P. Perfetti, A. Cricenti, J. Alloys Compd. 401 (2005) 80–85.
[36] J. Generosi, G. Margaritondo, J.S. Sanghera, I.D. Aggarwal, N.H. Tolk, D.W. Piston, A. Congiu Castellano, A. Cricenti, Appl. Phys. Lett. 89 (2006) 233906.
[37] J. Generosi, G. Margaritondo, M. Kropf, H. Hirling, S. Catsicas, K. Johnsson, N.H. Tolk, D.W. Piston, A. Cricenti, J. Appl. Phys. 104 (2008) 106102.
[38] J. Generosi, G. Margaritondo, J.S. Sanghera, I.D. Aggarwal, N.H. Tolk, D.W. Piston, A. Congiu Castellano, A. Cricenti, J. Microsc. 229 (2008) 259–263.
[39] D.W. Pohl, W. Denk, M. Lanz, Appl. Phys. Lett. 44 (1984) 651–653.
[40] G. Margaritondo, Surf. Rev. Lett. 2 (1995) 305–318.
[41] G. Margaritondo, G. De Stasio, Int. J. Imaging Syst. Technol. 8 (1997) 188–203.
[42] Y.-T. Chen, T.-N. Lo, Y.S. Chu, J. Yi, C.-J. Liu, J.-Y. Wang, C.-L. Wang, C.-W. Chiu, T.-E. Hua, Y. Hwu, Q. Shen, G.-C. Yin, K.S. Liang, H.-M. Lin, J.H. Je, G. Margaritondo, Nanotechnology 19 (2008) 395302.